
# *Scattering of X-rays in diagnostic radiology:*

*Computed radiography, digital radiography, mobile digital radiography and mobile C-arm fluoroscopy*

761683S, Master's Thesis

Satu Ylimaula
Research Unit of Medical Imaging, Physics and Technology
Research Unit of Nano and Molecular Systems, Biomedical Physics

University of Oulu
2021

# Abstract

The medical use of X-ray-based imaging modalities has increased in the last decade. During imaging scattered radiation is generated, and the staff can be exposed to it in various situations, including when holding the patient or conducting an interventional operation. To be able to minimize the exposure it is essential to have knowledge of the distribution of the scattered radiation. In this study scattered radiation maps where implemented based on direct measurements with dosimeters in various distances, angles and heights using an anthropomorphic phantom as a scattering object. Measurements were done using multiple imaging modalities and parameters. Maps were intended for educational purposes to be used in the radiation protection training of the staff.

Thorax PA and LAT measurements in a standing position demonstrated that the scattered radiation is directed strongly back from the phantom towards the X-ray tube. Scatter intensity being stronger in the LAT imaging. On the other hand, pelvis AP measurements in a supine position demonstrated that the radiation is directed relatively equally to all directions when the horizontal plane perpendicular to the primary beam central axis is considered. The use of the pelvic shield in Thorax measurements and the radiation protection blanket in Pelvis measurements did not affect scattering with the applied measurement method. Also using 50kg weighing child's imaging parameters did not have effect on the scattering as the same phantom was used.

Measurements done using fluoroscopy with urological experiment parameters demonstrated that the scattered radiation is directed relatively equally to all directions when the horizontal plane perpendicular to the primary beam central axis is considered. However, there is an emphasis on the scatter at the end of the patient table where the operating physician would be positioned, and accordingly a decrease on the scatter at the opposite end. The use of the lamella radiation protection curtain on the physician's end of the operation table decreased the measured dose rates of the dosimeter, that was placed lower than patient table surface level and therefore was shielded by the curtain.

Bedside Thorax measurements with a mobile imaging system demonstrated that the scattered radiation is directed relatively equally to all direction when the horizontal plane perpendicular to the primary beam central axis is considered. Also, when these measurements are compared to the previous stationary Thorax measurements, it is evident that scattered radiation dose rates with the mobile system are lower.

As the used dosimeter system measures personal dose equivalent $H_p(10)$ rate, the cumulative dose values calculated based on the exposure time can be used as an estimate of the overall effective dose. Dose received by the healthcare professionals is small in Thorax and Pelvis imaging in a possible holding situation when compared to the annual dose limit of radiation workers. On the other hand, the estimated dose of the physician is clearly higher in a fluoroscopy-guided urological operation. Yet the magnitude of the physician's dose is on the level that it is unlikely to exceed the annual dose limit. Lowest estimated effective doses were gotten in the bedside Thorax examination, where the dose received by the personnel correspond to 12 and 8 seconds of background radiation on 0.7- and 1-meter distances to the scatter radiation origin, respectively.

# Contents

# Introduction

The benefits of the medical use of ionizing radiation are indisputable, and this has led to an increasing use of the radiation-based imaging techniques in the healthcare. In Finland during the last decade, between years 2008 and 2018, the increase in the number of the plain radiographic exams was 49.8 % (due to increase in number of dental X-ray examinations), in the computed tomography exams 74.5 % and in the radiological procedures 48.8 %. During the same period, the collective effective radiation dose per Finnish citizen due to the medical radiation usage increased from 0.45 mSv to 0.72 mSv (Ruonala V. 2019, Siiskonen T. 2020, Zanzonico P. et al. 2016).

The medical exposure to the ionizing radiation increases the risk of cancer of the patient. Even though this increase in the risk is small, all medical use of ionizing radiation should comply with ALARA principle, which states that the exposure should be "As low as reasonably achievable". In addition to the patient, also healthcare professionals can be exposed to the radiation, for example, when they help or hold the patient during imaging. Especially the physicians performing fluoroscopically guided procedures are exposed constantly to substantial amounts of radiation, as they need to stand close to the patient and the X-ray tube. Additionally, these procedures tend to be lengthy, which further increases the physician's dose. Although the dose received by the staff is small compared to the patient's dose, the cumulative dose during a long work career can be significant. (Chida K. et al. 2012, Kwang P.K. et al. 2012, Sequeiros R.B. et al. 2017)

The radiation dose of the patient and healthcare professionals can be minimized by following radiation protection guidelines. Proper training is an essential part of these. In Finland, the arrangement of radiation protection training for the radiation workers is registered as part of the radiation law, and the Finnish Radiation and Nuclear Safety Authority (STUK) monitors that this duty of the employer is obeyed. Based on the EU directive 2013/59/EURATOM, similar training practices are required in all EU countries. (Bartal G. et al 2014, Eur-lex 2020, Finlex 2020b, Jentzsch T. et al. 2015, Miller D.L. et al 2009)

Exposure of the radiation workers is mostly caused by the radiation scatter. Scattered radiation is generated by any object on the path of the primary beam. The primary source being the patient. To be able to minimize scattered radiation exposure, it is necessary to have knowledge of its distribution in the imaging room. It can be visualized either using simulations (Rodas N.L. & Padoy N. 2015, Süncksen M. et al. 2020, Wagner M. et al. 2012) or by making wide direct measurements using

dosimeters (Nakamura T. et al. 2020, Nowak M. et al. 2020). Based on the literature review, the number of wide direct measurements done in this decade is relatively low, and the methods and parameters used in the reviewed articles differ from the ones used in this study. (Chida K. et al. 2011, Jentsch T. et al. 2015, Rodas N.L. and Padoy N. 2015, Wagner M. et al. 2012)

The purpose of this study was to implement scattered radiation maps in three imaging rooms at the Oulu university hospital. These maps were intended for educational purposes for the radiation protection training, and so different kind of imaging modalities and imaging programs were used in the measurements to identify the spatial distribution of the scattered radiation in various situations. Also, as radiation intensity is inversely proportional to the square of the distance of the scattered radiation origin, increasing distance to the radiation source (patient) is one of the fundamental methods used in radiation protection. These maps visualize the effect of the distance to the radiation intensity to the staff. An additional purpose of this study was to estimate the exposure of the staff in a different situation, such as when holding the patient during imaging or when conducting a fluoroscopy-guided operation.

# Theory

## 1. Ionizing radiation

An atom is an electrically neutral unit, which composes of neutrons, protons and electrons. The first two of these form a positively charged nucleus that is circled by negatively charged electrons. When an atom receives or loses an electron, it becomes an ion that has a negative or positive charge respectively. This process is called ionization. (Carroll Q.B. 2018, Franklin K. et al. 2010)

Electromagnetic waves can be divided into seven groups based on their energy and interaction with matter (*Table 1*). From these groups, X-rays and gamma rays are classified as ionizing, as they have high enough energy to cause ionization in atoms by freeing electrons from the atomic shells. When considering interaction with matter, X-rays can be thought to compose of massless particles called photons. According to Einstein, photons are a packet of energy that have both wave properties and properties of the energy defined by Planck's law. Planck's law states that photon's energy can be calculated as a multiplication of Planck's constant (h) and photon's frequency (f):

$$E = hf = \frac{hc}{\lambda}, \quad [1]$$

where $c$ is the speed of light in vacuum and $\lambda$ is photon's wavelength. (Alpen E.L.1998, Sequeiros et al. 2017)

***Table 1.*** *Seven types of electromagnetic waves and their wavelength magnitude (Alpen E.L.1998, Sequeiros et al. 2017).*

| **Radiation** | **Wavelength** |
|---|---|
| Radio waves | ~ 1 meter to kilometers |
| Microwaves | ~ 0.1 millimeters to 1 meter |
| Infrared light | ~ millimeters to micrometers |
| Visible light | ~ hundreds of nanometers |
| Ultraviolet light | ~ hundreds of nanometers, but less than visible light |
| X-rays | ~ $10^{-8}$ meters or less |
| Gamma rays | ~ $10^{-10}$ meters or less |

How radiation interacts with matter depends on the atomic number of the medium and the energy of the radiation. When considering X-ray energies used in radiography, the principal interaction methods are a photoelectric effect and a Compton scatter. In the photoelectric effect, the photon transfers all its energy to an electron, which as a result is released from an atom. The kinetic energy of the

photoelectron is defined as a subtraction of photon energy and electron binding energy. The vacant place on the atomic orbital is then filled with an electron from a higher atomic orbital resulting in characteristic X-rays or Auger effect in which outer shell electron is ejected from the atom as an Auger electron. On the other hand, in the Compton scattering X-ray photon collides with a loosely attached outer shell electron and as a result part of photon's energy is transferred into the electron. Electron is ejected from the atom and photon is deflected from its course. (Cherry S.R. 2012, Dance et al. 2014, Martz et al. 2017, Sequeiros et al. 2017)

In addition to photon energy, the interaction of photons with the medium depends on the atomic number of the matter. When atomic number increases the probability of interaction increases, i.e. heavier atoms attenuate more radiation. Bones contain a lot of calcium and phosphorus atoms, while muscle comprises of lighter atoms such as hydrogen, carbon and oxygen. Consequently, bones interact more likely with the X-rays and appear white on the X-ray image. (Wolbarst 1999)

### *1.1 Biological effects of ionizing radiation*

Interaction of X-rays with the matter causes "free radicals", i.e. atoms or molecules with unpaired electron on the outer electron shell. These free radicals can damage cells in three ways: molecular bonds can break; protein molecules may become non-functional and cellular DNA may get damaged. If the damage happened on the DNA, it can be characterized as somatic or genetic depending if the damage is non-inheritable or inheritable. Non-inheritable damages increase the risk of cancer of the exposed individual. Inheritable damages happen on the reproductive cells and can be therefore transferred on to next generations. (Franklin et al. 2010)

Overall biological effects of ionizing radiation can be divided into tissue reactions (formerly named as deterministic) and stochastic effects. Tissue reactions happen quite shortly after exposure, they have a threshold dose value, and the severity of the reactions increase with increasing dose. Only radiation doses, that can cause cell death in an extent that the organ function reduction is evident, can cause tissue reactions. *Table 2* comprises examples of tissue reactions and their threshold dose values. (Franklin et al. 2010, Statkiewicz Sherer et al. 2018, STUK 2009)

On the other hand, stochastic effects occur in delay and they do not have threshold value. They are caused by cellular or DNA damage that is not deathly to the cells. For this reason, the effects are dependent on the cell repair mechanisms and so the severity of the effects does not increase with

increasing dose. However, the probability of effects increases when the dose increases. For example, a cancer is a stochastic effect. (Franklin et al. 2010, Statkiewicz Sherer et al. 2018)

***Table 2.*** *Tissue reactions and their threshold dose values. (STUK 2009)*

| **Whole body dose [Sv]** | **Reaction** |
|---|---|
| 0,5 | Blood count change in few days |
| 1,0 | Nausea in few hours |
| 4 | Life-threatening dose. Patient can still be saved with good medical care |
| 10 | Patient can't be saved even if good medical care is given |
| **Local skin dose [Sv]** | **Reaction** |
| 6 | Redness in few hours |
| 15 | Vesicles in couple of weeks |
| 20 | Gangrene |

As tissues, that have high mitosis rate, are more vulnerable to ionizing radiation, children have higher risk of getting stochastic effects from radiation exposure. Generally, this risk is considered to be 3 to 4 times the risk of adults. The risk is highest in early childhood and it gradually decreases during adolescence to correspond the risk of adults (Alzen G. & Benz-Bohm G. 2011, Sequeiros et al. 2017).

### *1.2 Sources of ionizing radiation*

According to the Radiation and Nuclear Safety Authority of Finland (in Finnish Säteilyturvakeskus, for short STUK) the mean effective dose of ionizing radiation received by Finnish citizen is 5.9 mSv per year per person. *Figure 1* specifies all the contributors of this dose. Major part of it is caused by natural background radiation, which includes exposure to inside air radon (4 mSv) and other natural background radiation sources (~1.1 mSv) like cosmic radiation, soil, construction materials, food, water and traveling by flying. The rest is mainly due to the use of ionizing radiation in the medicine, therefore medical imaging is by far the biggest manmade contributor to the annual dose. (Siiskonen T. 2020)

In addition to the radiation sources mentioned in previous the chapter, it is also possible to be exposed to ionizing radiation at work. Flight operation industry, nuclear power production and healthcare are the biggest fields where exposure is possible. During 2019 there were 4598, 4101, and 4141 people, respectively, working in these fields in Finland. (STUK 2020b)

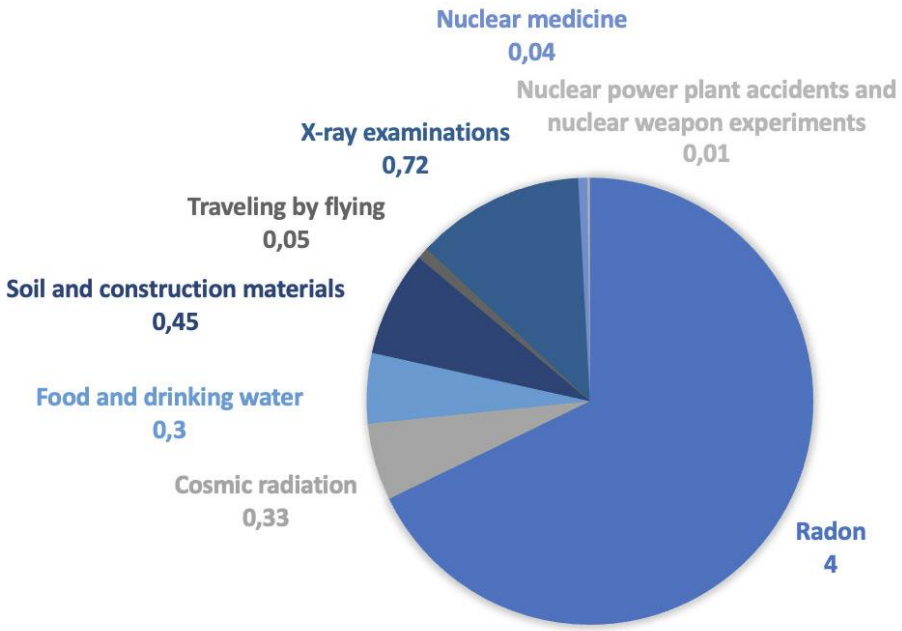


***Figure 1.*** *Contributors to the mean annual effective dose of ionizing radiation received by each Finnish citizen. Values presented are in millisievert (Siiskonen T. 2020).*

## 2. X-ray imaging from 19th century to date

### *2.1 Beginning of radiography*

In 1875 Sir William Crookes invented so called Crookes tube, which consists of a partly evacuated glass tube inside which are two or more electrodes. When high voltage is applied between the electrodes, the residual gas inside the tube is ionized. Generated positive ions head towards negative cathode plate and collide with it. This causes electrons to release from cathode. Negatively charged electrons are directed almost perpendicularly away from the cathode and when hitting the other end of the glass tube they induce fluorescence. As the rays causing fluorescence emerged from the cathode, they were first called cathode rays. (Carroll Q.B. 2018, Martz et al. 2017)

November 8th 1895 Wilhelm Röntgen was experimenting above described cathode rays in his laboratory at the University of Würzburg. He had covered the tube with a black cardboard and the room was darkened. During his experiments he noticed that a barium platinocyanide coated paper, that was placed on a nearby bench, was glowing. He soon realized that the glowing was not caused by the cathode rays but some other radiation. He named the radiation as X-rays, as it was an unknown factor. This experience inspired Röntgen to conduct thorough experiments with these new rays on the following weeks. (Als-Nielsen et al. 2011, Carroll Q.B. 2018, Martz et al. 2017, Nicholls M. 2019, Wolbarst A.B. 1999)

Röntgen published his research results of X-rays in December 1895 on a local scientific paper. This publication included also the famous first radiographic image Röntgen had taken of his wife's hand (*Figure 2*). Results quickly awakened interest around the globe and on January 1896 many reputable scientific journals reported of this discovery, including Scientific American and NATURE. Altogether 49 books and over 1000 technical articles were published of X-rays during the year 1896. Röntgen was awarded Nobel prize in 1901 for his discovery of the X-rays. (Als-Nielsen et al. 2011, Anonymous 1896, Carroll Q.B. 2018, Martz et al. 2017, Röntgen W.C. 1896)

Within a year from Röntgen's discovery an American scientist Thomas Edison developed a device called "fluoroscope", which enabled functional X-ray imaging of patients in real-time. Unfortunately, doctors and patients received quite high radiation doses when using fluoroscope. This was noticed also by Edison. Nevertheless, very similar fluoroscopes remained in medical usage for over fifty years. Finally, in 1948 John Coltman developed an electronic intensifier that decreased considerably the radiation dosage needed for fluoroscopic imaging. (Carroll Q.B. 2018, Martz et al. 2017, Mikla et al. 2014)

Overall advancements in electronics and computers made rapid developments of x-ray imaging methods possible starting from the 1970s. Computed radiography (CR), in which the imaging cassette is scanned afterwards with laser beam and the image is converted into electrical form, became commercially available in the beginning of the 1980s. Direct capture digital radiography (DR) followed right behind in the 1990s. It transformed the whole imaging process into digital. (Carroll Q.B.2018)

Advancements in CR and overall electronics enabled also development of computed tomography (CT). In CT transmission profiles of patient are acquired from several directions and these profiles are then reconstructed into sequential CT images which enable 3D localization of the structures presented on the images. Already in 1917 had John Radon published an article that specified the method for reconstructing a function from several image projections. Today this inverse transformation process is called Radon transform. But it took till 1970's that Radon's mathematical methods were used to form CT imaging by Hounsfield and Cormack. First CT image of patient was taken 1972 in England and by the beginning of 1980s there were over 5000 CT scanners in use worldwide. Hounsfield and Cormack received Nobel Prize in 1979 for their development work of the CT. (Martz et al. 2017, Mikla et al. 2014, Radon J. 1986)

***Figure 2.*** *First radiographic image that was included on the Röntgen's original publication presenting the discovery of x-rays. Röntgen took the image of his wife's hand. (Figure used with permission from Röntgen W.C. 1896)*

### *2.2 Principle of X-ray production*

X-rays are produced in an x-ray tube (*Figure 3*). The tube is made of glass and it contains a negatively charged cathode and a positively charged anode, which are encased in a vacuum space. The cathode comprises of a focusing cup and a filament. In modern X-ray tubes there are usually two filaments of different sizes positioned inside the focusing cup, small and large. Selected filament is heated with electrical current, which makes the electrons on the filament material move faster and more freely around the atom nucleus. The heating current corresponds to the tube current value given by radiographer from the control panel. When high voltage is applied between the anode and the cathode, electron flow from the cathode to the anode is induced. Negatively charged cathode cup walls focus the electron stream into a small area on the anode, which is called a focal spot. Before imaging radiographer selects wanted focal spot size and the filament to be used is selected accordingly. The small filament produces smaller focal spot than the large filament. The focal spot size is relative to the exposure of a patient. Smaller focal spot is usually used when imaging smaller body parts and large when imaging larger. (Carroll Q.B. 2018, Ehrlich et al. 2017)

When the electron stream strikes anode, over 99% of the radiation produced is emitted as a heat and a visible light. Consequently, the anode needs to withstand high temperatures and therefore it is made of tungsten, which has a high melting point. To further improve the anode's tolerance of heat, the anode disc is rotated. This way the formed heat is distributed over a larger area. To guide the x-rays emitted from the anode towards the tube's window, the anode disc is inclined 6° to 22° from its edges.

The choice of the best angle is a balance between a heel effect and a focal spot size. The heel effect means that when the travel distance of x-rays inside anode material increases the exited x-rays' intensity decreases, i.e. heel effect causes positional alteration on the intensity of the radiation that is emitted from the x-ray tube. When the angle of anode edge inclination is bigger heel effect is decreased but focal spot size increases and vice versa. (Carroll Q.B. 2018, Dance et al. 2014)

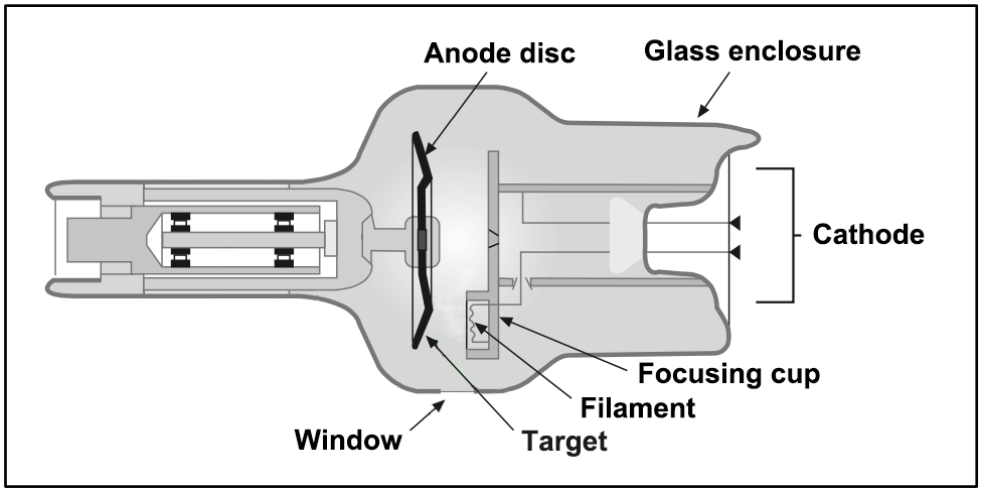


***Figure 3.*** *Scheme of an X-ray tube structure. (Figure modified with permission from STUK 2004)*

Less than 1% of the radiation, that is emitted from the anode, is emitted as X-rays. The X-rays are produced in two ways. If the incoming electron interacts with the anode material's atomic nucleus, the electron decelerates and loses its kinetic energy. The lost energy is emitted as an X-ray photon. The energy of the emitted photon is dependent of the distance between the atomic nucleus and the electron. This dependence is caused by the Coulomb forces, which get stronger with decreasing distance between the nucleus and the electron. As the X-rays originate from the electron deceleration, they are called a bremsstrahlung, which means braking radiation in German. As a result of the bremsstrahlung, a heterogeneous X-ray beam with variety X-ray energies, is produced. (Carroll Q.B. 2018, Dance et al. 2014)

Second possibility of producing X-rays is, if the electron, coming from the cathode, passes nearby the anode material's orbital electron. If the passing electron's kinetic energy is higher than the binding energy of the orbital electron, it can eject the orbital electron out of its electron shell. After collision the passing electron continues with a decreased energy and a changed direction. When the vacancy, left by an ejected electron, is filled by an outer orbital electron, an X-ray photon is produced. Energy of the photon corresponds with the binding energy difference of the vacancy and the filling electron's

original location. Consequently, X-rays produced in this manner are monoenergetic and characteristic for the anode material.

*Figure 4* presents illustration of an X-ray spectrum that includes the heterogenous bremsstrahlung and the monoenergetic characteristic radiation. Characteristic radiation peaks are named according to the electron shell where the vacancy was (K, L, M, N…) and according to distance of the shell where the filling electron came. For example, if the vacancy was in the K-shell and the filling electron came from the L-shell, then the characteristic radiation peak is called $K_\alpha$. If the same vacancy was filled with an electron from M shell, then the peak would be called $K_\beta$. In other words, if the filling electron came from neighbouring electron shell, then the subindex of transformation name is α, and if it came from further, it is β. (Carroll Q.B. 2018, Dance et al. 2014)

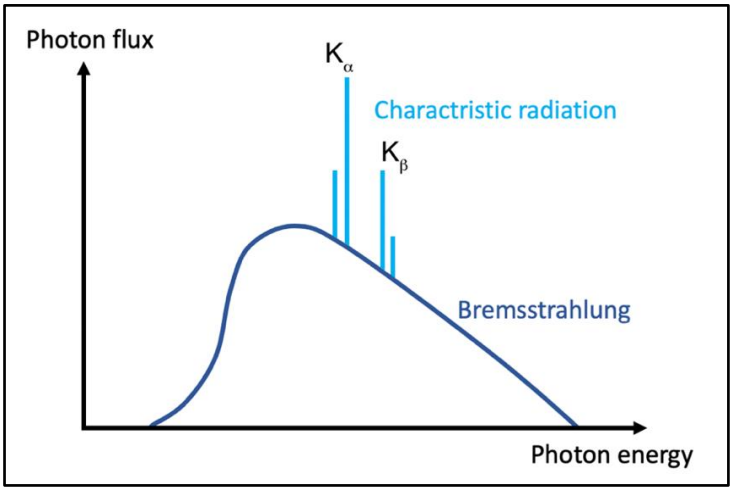


***Figure 4.*** *Illustration of an X-ray spectrum produced in the X-ray tube. The spectrum includes continuous bremsstrahlung radiation and discrete characteristic radiation. The characteristic radiation is named as a $K_\alpha$ and a $K_\beta$ corresponding to the electron transmission from L and M -shells into the K-shell vacancy respectively. (Figure drawn based on Carroll Q.B. 2018 and Dance et al. 2014)*

### *2.3 X-ray based imaging modalities today*

Approximately 6 million X-ray examinations and procedures were done in Finland in 2018. From those 88.3 % were plain X-ray examinations and contrast agent examinations, 9.5 % CT examinations, 0.9 % fluoroscopy during surgical operations, 0.6 % angiographic examinations and 0.7 % cone-beam computed tomography (CBCT) examinations, which are commonly used in dentistry. In this chapter basic concepts of the most used healthcare X-ray imaging modalities are reviewed. (Ruonala V. 2019)

*2.3.1 Radiography*

Radiography is sometimes referred also as a plain radiography or a projection radiography. It compasses a projection image of an 3D object taken in a 2D format. As the X-rays origin from a point like source and spread as they proceed from the X-ray tube to the image receptor, the resulting image contains geometrical distortions. For example, all objects or body parts are magnified on the image, and the magnitude of the magnification is dependent on the distance between the object and the image receptor. For this reason, a thorough training is needed on the interpretation of the radiographs. (Dance et al. 2014)

For an X-ray image, the patient is positioned in front of the image receptor (*Figure 5*). Originally these receptors contained a radiographic film, but today film systems have been replaced by digital modalities. There are two optional methods for the digital imaging: computed radiography (CR) and digital radiography (DR). In CR a cassette containing a phosphor layer is used instead of film to store a latent radiograph. Afterwards the cassette is scanned with a laser to convert the latent image into a digital form. In DR direct digital storage of the radiograph is enabled with the use of a scintillator-based flat detectors. The operating principles of CR and DR image receptors are presented in more detail in chapter 2.4. (Ehrlich et al. 2017, Sequeiros et al. 2017)

After positioning the patient in front of the image receptor, the X-ray tube is aligned with the centre of the image receptor and the imaging properties are selected from the control panel. The selected imaging properties include collimation, tube current, tube voltage peak -value, exposure time, and use of grid and filter. Of these collimation limits the radiated area, tube current determines the X-ray flux, tube voltage peak -value determines the energy range of the produced X-rays (*Figure 6*) and the exposure time determines the length of exposure. Additionally, grid can be used to remove scattered radiation from the X-ray beam reaching the receptor, and filter to modify the X-ray spectrum reaching the patient optimal and concurrently minimize the unnecessary patient exposure. (Carroll Q.B 2018, Ehrlich et al. 2017)

When the exposure is turned on, the so-called primary beam of the X-rays travel from the X-ray tube through a filter and a collimator to the patient. Photons interact with the patient's body and continue as a partly scattered remnant beam to the image receptor through the grid. Radiation, that is scattered inside the patient, is orientated to all directions, but a part of it goes toward the image receptor and can be removed with the use of grid. (Carroll Q.B. 2018, Ehrlich et al. 2017, Sequeiros et al. 2017)

Manually setting the imaging properties is quite challenging task and it easily leads to an inconsistent exposure of the patients and a varying image quality. This can induce unwanted re-examinations. To avoid these situations, present x-ray imaging systems include an automatic exposure control (AEC). The AEC is located behind the image receptor and it records the photon flux that has transmitted the patient and the image receptor. When adequate number of photons have reached the image receptor, AEC ends the exposure. (Carroll Q.B. 2018, Dance et al. 2014)

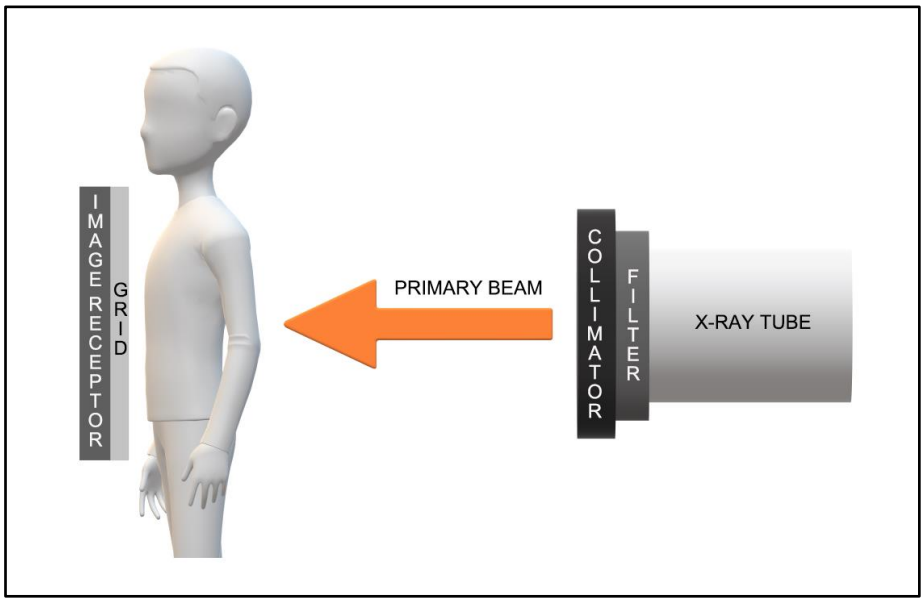


***Figure 5.*** *The basic structure of the X-ray imaging system. X-rays are produced on the X-ray tube, from where they travel as a primary beam through the filter and the collimator to the patient. After passing the patient the so-called remnant beam is captured by the image receptor, which is positioned behind the grid. The grid removes unwanted scatter from the beam.*

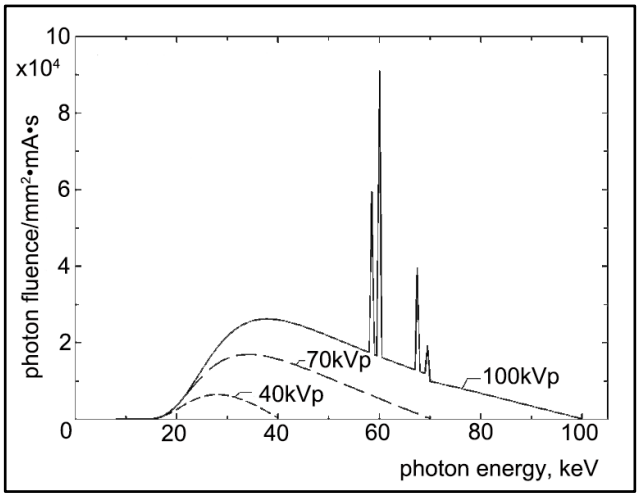


***Figure 6.*** *The effect of the selected tube voltage peak -value to the spectrum of the produced X-rays. The higher the peak voltage the wider the photon energy range produced. The selected tube current -value doesn't have effect on the spectrum shape, but it determines the photon flux. (Figure modified with permission from Dance et al. 2014)*

*2.3.2 Computed tomography*

Computed tomography (CT) is a widely used rapid three-dimensional imaging method. The main parts of the CT system are a gantry and a movable patient table (*Figure 7 a*). Gantry is a cylindrical imaging assembly that includes for example the X-ray tube, detector elements, collimators and filters. Additionally, the gantry contains the whole rotation mechanics and a powerful cooling system, which enables the fast three-dimensional imaging. Differing from the radiography, the X-ray beam used for imaging is shaped as a fan or a cone beam to correspond to the shape of the detector, that is line like and composes of tens or hundreds of detector rows each containing hundreds of detector elements. (Dance et al. 2014, Sequeiros et al. 2017)

When a CT image is taken, a set of transmission profiles through the patient are acquired by rotating the x-ray tube and the detector around the patient. In a conventional axial CT, the data of transmission profiles are acquired, and then the patient table moves to the position of the next slice (*Figure 7 b*). Newer systems enable a spiral/helical imaging in which the patient table is constantly moving while the X-ray tube and the detector rotate around the patient (*Figure 7 c*). (Dance et al. 2014, Smith et al. 2014, Sequeiros el al. 2017)

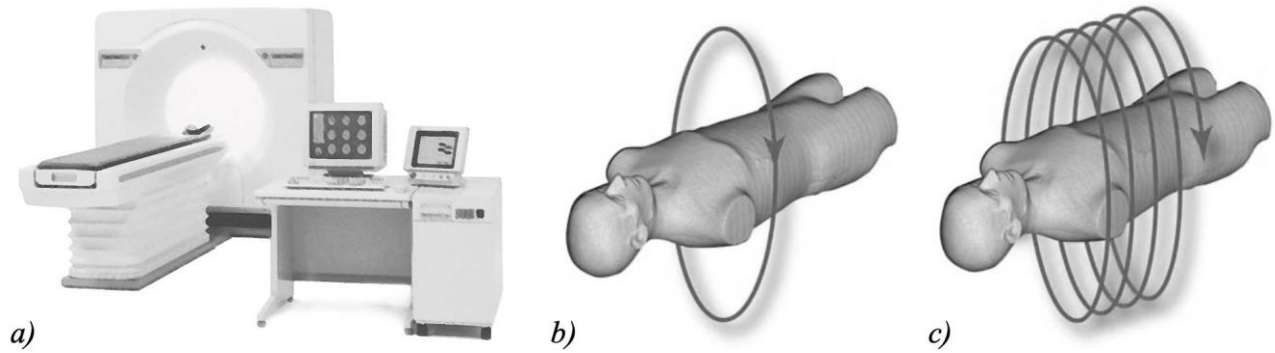


***Figure 7.*** *a) A CT scanner illustration. Main parts of the scanner are the gantry and the patient table. b) A visualization of the manner in which the CT transmission profiles are acquired in the axial imaging. c) A visualization of the manner in which the CT transmission profiles are acquired in the helical imaging. (Figure a) used with permission from STUK 2004 and figures b) and c) used with permission from Dance et al. 2014)*

As in the radiography, also in the CT part of the photon beam, that passes through the patient, is attenuated either by the absorption or by the scattering. Amount of the attenuation is dependent on the atomic number of the matter and the photons energy. Attenuation obeys the Beer's law:

$$I(x) = I_0 e^{-\mu x}, \qquad [2]$$

where $I_0$ is the intensity of the unattenuated X-ray beam, $x$ is the thickness of the material, $\mu$ is the linear attenuation coefficient of the material and $I(x)$ is the intensity of the attenuated X-ray beam that has passed through the matter in question. (Dance et al. 2014)

The reconstructed CT image is formed as a matrix of pixels. Pixels represent corresponding three-dimensional voxels of the scanned CT slice. It is possible to determine a linear attenuation coefficient for each pixel based on the Beer's law, when the attenuated and the unattenuated beam intensities are known. But as the human body is made of variety of tissues having different attenuation properties, the Beer's law gets a form:

$$I(d) = I_0 e^{-\sum_{i=1}^{i=n} \mu_i \Delta x}, \quad [3]$$

where $n$ is the number of the pixels in the direction of the beam, $\Delta x$ is the length of the pixel and $I(d)$ is the intensity of the attenuated X-ray beam, that has passed the patient. (Carroll Q.B. 2018, Dance et al. 2014)

As polyenergetic X-rays are used in the CT imaging, the Beer's law should be integrated over all photon energies. In practise this is not done, but instead an average of photon energies is used. This can cause beam hardening artefact in the image, if the scanned area includes objects that attenuate the X-ray beam strongly, like a compact bone or a metal object. Calibration of the machinery with a phantom is done to diminish the beam hardening effect. (Dance et al. 2014)

The actual transformation of the transmission profiles, i.e. attenuated intensity values, into a CT image is done by using a filtered back projection method. This includes four phases. First, the Radon space often named as a sinogram, that consists of acquired projection profiles, is Fourier transformed (FT). Second, a high pass filter is applied on the calculated FTs. Third, filtered FTs are inverse Fourier transformed back into the Radon space. Fourth, filtered projection profiles are back projected to reconstruct the CT image. *Figure 8* presents CT images reconstructed with different amounts of transmission profiles. It can be seen that when the amount of transmission profiles increases the accuracy of the final back projected image increases as well. (Dance et al. 2014)

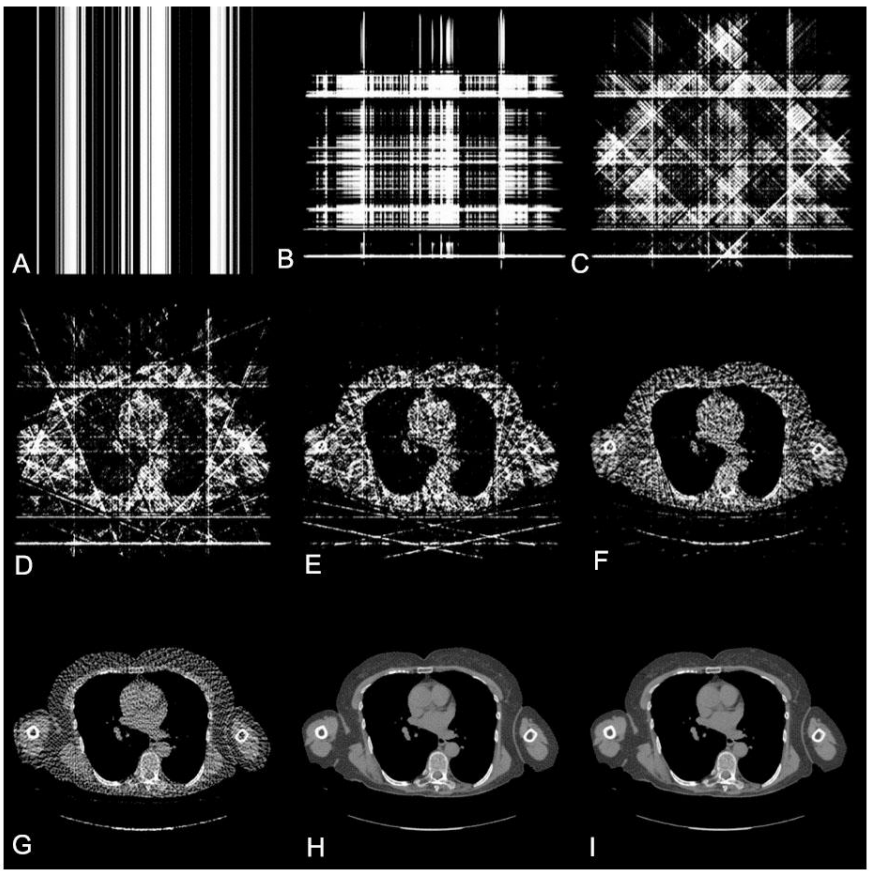


***Figure 8.*** *CT images reconstructed using filtered back projection. Number of acquired transmission profiles were A) 1, B) 2, C) 4, D) 8, E) 16, F) 32, G) 64, H) 256 and I) 1024. (Figure used with permission from Dance et al. 2014)*

In the final CT image, the linear attenuation coefficients are converted into a Hounsfield unit scale, which presents the attenuation relative to the water at a room temperature:

$$HU_{material} = \frac{\mu_{material} - \mu_{water}}{\mu_{water}} \times 1000, \qquad [4]$$

where $\mu_{material}$ and $\mu_{water}$ are the linear attenuation coefficients of the matter in question and water respectively. (Dance et al. 2014)

*2.3.3 Fluoroscopy*

Fluoroscopy is an imaging modality in which dynamic real time images are produced. Images are analysed simultaneously as they are produced, and for this reason the experiment is usually conducted by a radiologist and not a radiographer as in other imaging modalities. Fluoroscopy is used to view processes or instruments inside patient's body during different kind of procedures such as gastrointestinal, vascular or interventional procedures. As these procedures can be lengthy, the

emphasis on the image quality is to keep it at a sufficient level while simultaneously keeping the patient dose level as low as possible. For this reason, the contrast is usually low and the noise high in fluoroscopic images when compared to the other imaging modalities. (Carroll Q.B.2018, Dance et al. 2018, Ehrlich et al. 2017)

The overall mechanical structure of the fluoroscopic imaging system can vary depending on the use purpose, but generally systems are single plane and configured so that the X-ray tube is located under the patient table and the detector above it (*Figure 9 a*). For example, in the interventional cardiology and radiology the fluoroscopic device is constructed as a C-arm in which X-ray tube and detector are fixed so that their distance with respect to each other can't be changed. The position and the angle of the C-arm in respect to the patient can be changed quite freely, by rotating the C-arm or by moving the patient table that is usually cantilevered. In some special cases it is necessary to acquire two projections, and in these situations a biplane fluoroscope can be used. It is constructed of two C-arms and both C-arms can be freely rotated and positioned with respect to each other (*Figure 9 b*). (Dance et al. 2018)

For a long time, fluoroscopic imaging devices were based on an image intensifier tube, which was introduced in the late 1940's. The image intensifier enabled a lower radiation dose to be used on the imaging compared to the previous methods and hence decreased dramatically radiation doses received by the patients and the operators. Today the image intensifier -based systems have been mostly replaced by the digital systems that include similar digital flat panel detectors as are used in radiography. These new generation devices enable use of a pulsed mode fluoroscopy, in which series of very short pulses of radiation are used for the image acquisition. Between pulses the patient is not radiated. Compared to a continuous mode fluoroscopy, the pulsed mode spares the patient of the unnecessary exposure of the radiation between consecutive images. It also improves the image quality, by diminishing the motion blur due to the short integration time. Other major benefit of the digital imaging is that it enables fast image modulation. For example, the digital subtraction angiography (DSA) is a fluoroscopic image modulation technique in which two consecutive images are acquired without and with contrast agent. Acquired images are log transformed and subtracted from each other to form an image where only the blood vessels including the contrast agent are visible. (Carroll Q.B. 2018, Dance et al. 2018)

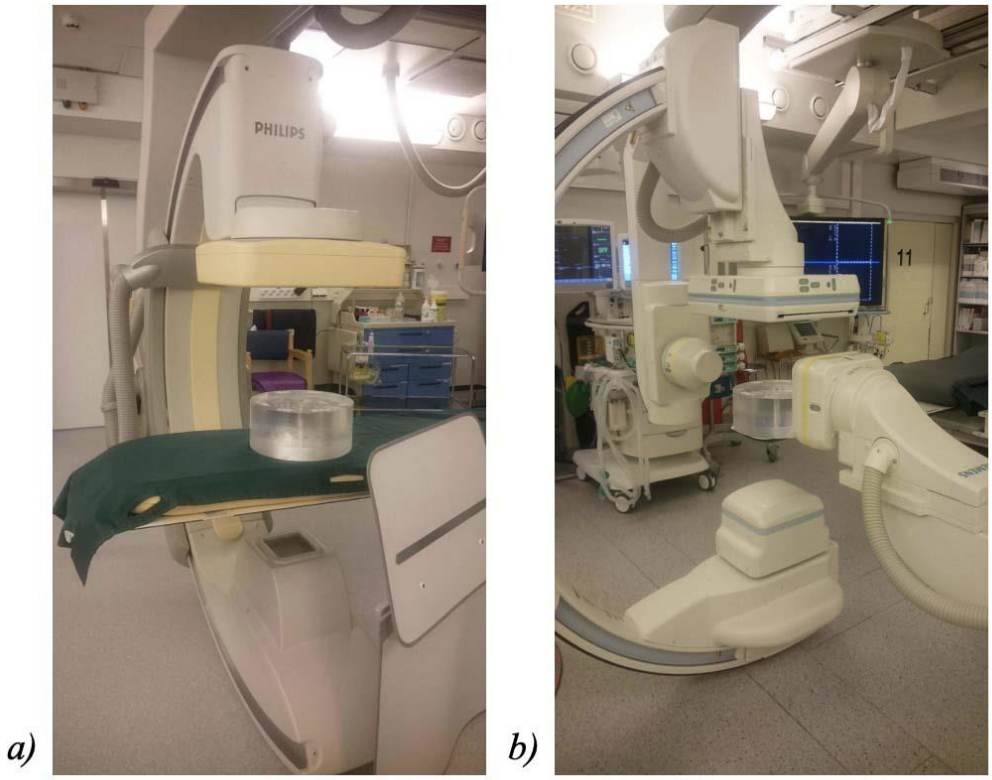


***Figure 9.*** *Examples of fluoroscopes used in the interventional radiology: a) A single plane C-arm and b) A biplane system with two C-arms.*

*2.3.4 Angiography*

Angiography refers to all imaging examinations that present blood vessels. Used imaging method can be for example radiography or fluoroscopy depending on the use purpose of the images. Regardless of the imaging method, in all angiographic examinations a contrast agent is used. This is generally a water-soluble iodine-based compound when X-ray based imaging method is used, and it is commonly given to a patient through a catheter during the examination. To acquire the actual angiographic images a timed sequence of images is taken. Depending on the experiment purpose the images are taken either prior to contrast agent dissemination and after it, or during dissemination and after it. Commonly used method acquiring angiographic images is digital subtraction angiography (DSA), which was described in the chapter where fluoroscopic methods were discussed. (Ehrlich et al. 2017)

*2.3.5 Mammography*

Mammography is an imaging method where a special equipment is used to image the breast. Main parts of the mammographic imaging system are the X-ray tube, image receptor, compression plate, breast support and grid (*Figure 10 a*). These are all integrated in an imaging unit, that can be rotated and height adjusted to enable the imaging angle modification and suitability for patients of varying

tallness. As in other X-ray imaging modalities, also in the mammography film-based systems have been replaced by the digital options during this millennium. Today similar image receptors, as are used in the computed radiography (CR) and the direct radiography (DR), are also exploit in the mammography. As basic requirements for a mammographic image are high soft tissue contrast and resolution to detect small details, DR based systems suite better to mammography as they enable more accurate images to be taken with lower radiation doses. Their disadvantage is that the deployment of the DR based system requires change of the whole imaging assembly unlike the CR. (Dance et al. 2018, Sequeiros et al. 2017)

During mammographic experiment the breast is compressed firmly between the compression plate and the breast support. This improves image quality and patient safety for several reasons. First, it reduces distance between the imaged object and the detector, which decreases both the scattered radiation reaching the image receptor and the geometric unsharpness. Secondly, compression decreases and uniforms the attenuation of the X-rays throughout the imaged area, which reduces radiation dose and exposure range. Thirdly, compression decreases unsharpness of the image caused by motion. (Dance et al. 2018)

Differing from other imaging modalities, mammography requires high soft tissue contrast and resolution. This is best accomplished by using a low energy radiation and a small focus size. The optimal radiation spectrum is achieved by setting the X-ray tube's peak voltage low, the imaging current high and the exposure time short. Filtering is used to further optimize the energy spectrum of the photons. To be able to image the whole area of the breast, the produced X-ray beam is collimated so that the central axis of primary beam becomes inclined in respect to orthogonal of the image plane (*Figure 10 b*). After collimation, the edge of the beam that is closest to the patient is orthogonal to the image plane and travels close to patient's chest to the edge of the image receptor. This way it is possible to image the whole breast starting from the chest plane of the patient. (Dance et al. 2018, Sequeiros et al. 2017)

A grid is an essential part of the mammographic device. Without a grid, 37-50 % of the radiation arriving to the image receptor would be radiation, that was scattered inside the breast. This would have a significant effect on the image quality by decreasing contrast and increasing noise. Use of the grid improves scatter to primary beam ratio substantially. For this reason, mammographic devices include a grid as a default. During imaging the grid is moved to avoid artefacts caused by the grid

septa. Septa is a wall like structure of the grid that permits only radiation parallel to the primary beam enter the image receptor. (Dance et al. 2018)

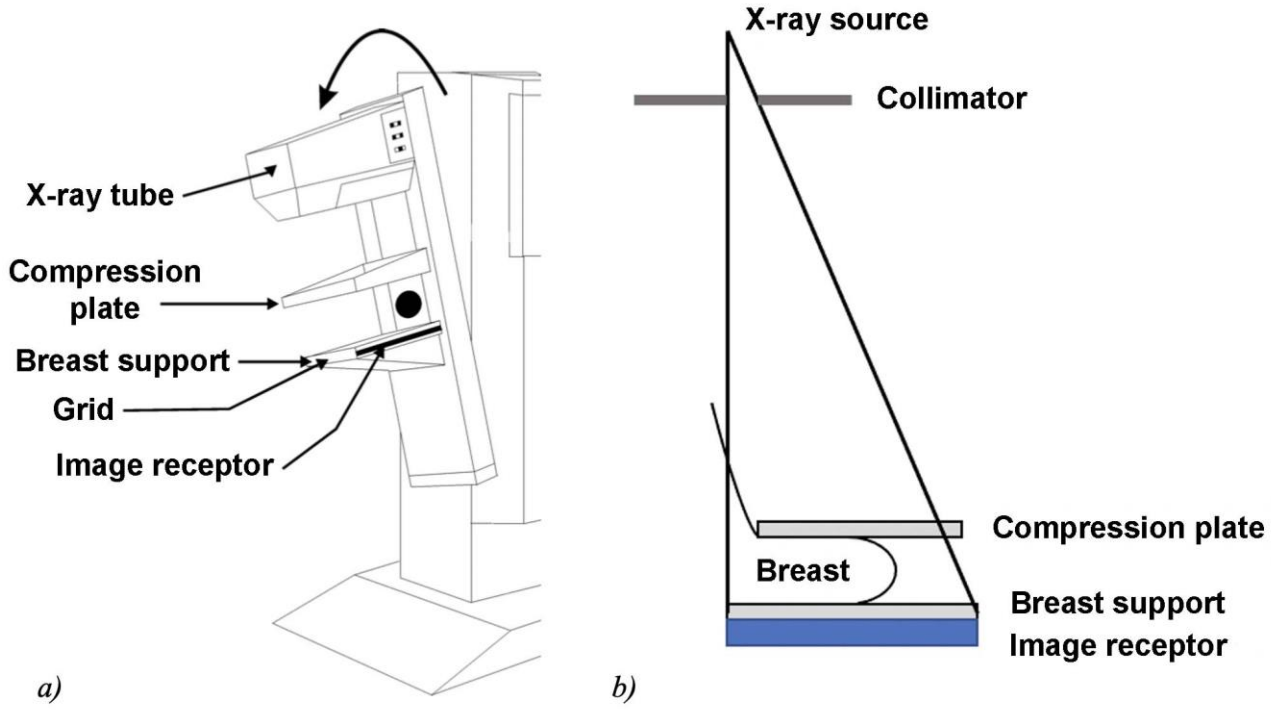


***Figure 10.*** *a) Schematic of the imaging device used in the mammography. b) Collimation used in the mammography to view the whole breast. (Figure a) used with permission from Dance et al. 2014)*

### *2.4 Modern X-ray image receptors*

As mentioned in previous chapters, modern X-ray based imaging systems include mainly two kinds of image receptors. These are the ones used in the CR and in the DR. Film-based imaging has in practice ended. This chapter will explain in more detail the basic structure and function of the image receptors used in the CR and the DR. (Mettler F.A. Jr. 2018)

#### *2.4.1 Computed radiography*

CR is a widely used digital X-ray imaging method. Its popularity partly stems from the fact, that conversion of the film-based system into the CR system requires only purchase of reusable CR imaging plates and an image reader. The actual X-ray imaging device, that was previously used with film-based imaging plates, doesn't need to be replaced. (Sequeiros et al. 2017)

The CR cassette's surface structure is usually made of aluminium or plastic. The front face of the cassette, through which the X-rays enter the image receptor, is made of low attenuation carbon fibre

and the back face may include a lead foil, to prevent backscatter of the radiation. The actual image receptor is positioned inside this shell and it includes a phosphor layer which is typically made of barium fluorohalide compound which has been activated with europium. Activation means that the europium changes the phosphor crystal's atomic structure creating metastable electron holes throughout it. When the X-rays enter the phosphor layer during image exposure, they cause ionization, i.e. electrons to be released from the phosphor material. These electrons are trapped in the metastable electron holes. The number of the trapped electrons depends spatially on the intensity of the incoming radiation and this way the so-called latent image is stored on the image plate. (Carroll Q.B. 2018, Dance et al. 2018, Sequeiros et al. 2017)

Latent image of the cassette is transformed into a digital form using an image reader. Readout is done by scanning the image receptor point by point with a red helium-neon laser. Stimulation with the laser causes electrons to be released from the metastable traps. When these released electrons are tide back to the electron shells, energy is liberated in a form of bluish light. Amount of the light is spatially proportional to the amount of radiation exposure of each point. The light is collected and guided optically into a photomultiplier tube, in which the signal is digitized and amplified. When readout of the whole image plate is finished, the image plate is flooded with light to release any remaining trapped electrons. After this the cassette is ready to be reused. (Carroll Q.B. 2018, Dance et al. 2014, Sequeiros et al. 2017)

### *2.4.2 Digital radiography*

DR is a form of imaging where a removable image cassette is not needed. Instead, an electronic image receptor is fixed on the X-ray system and transmits the captured image electronically into the processing computer. The image receptors used in DR are called flat panel detectors and they are based on the same technology which is used in flat panel displays. The receptor comprises of a matrix of small detector elements, that are often referred to as dexels or dels. Depending on the structure of these dexels, flat panel detectors can be divided into two groups: direct conversion and indirect conversion systems. (Carroll Q.B. 2018, Sequeiros et al. 2017)

The overall structure of the dexels is quite similar in direct and indirect conversion systems (*Figure 11*). The substrate is square shaped and in its opposite corners are positioned a capacitor and a thin film transistor (TFT). The capacitor stores the charge generated by X-ray exposure and transistor functions as a gate and release the charge when the dexel in question is read out. Most of the dexel's

space is reserved by the semiconductor detector area, which is sensitive to X-rays or light depending if the used system is direct or indirect conversion based. (Carroll Q.B. 2018, Mikla et al. 2014)

In direct conversion systems X-rays enter detector element through the top electrode and interact directly with the amorphous selenium semiconductor material (*Figure 12 a*). Semiconductor material is ionized, i.e. electrons are released and positively charged holes are generated. Freed electrons are attracted towards the positively charged top electrode and reciprocally positively charged holes accumulate on the bottom of the dexel, where the negatively charged dexel electrode is positioned. The positive charge of the holes is stored in the capacitor. The acquired charge is directly proportional to the intensity of the ionizing radiation. (Carroll Q.B. 2018, Dance et al. 2014, Mikla et al. 2014, Spahn M. 2013, Sequeiros et al. 2017)

The dexel structure of the indirect conversion system differs from the direct conversion system in two ways (*Figure 12 b*). First, the semiconductor used is amorphous silicon and secondly, the dexel matrix is coated with a cesium iodide scintillation layer. During exposure the X-rays interact with the scintillation layer, which causes generation of electron-hole pairs. When electrons fall back into atomic shells, energy is released in a form of visible light. Intensity of the released light is proportional to the intensity of the coming X-rays. Scintillation light is directed mostly towards dexels due to column like structure of the scintillation layer. Dexels function as photodiodes by converting this light into electrical charge in a similar manner as in the direct conversion method. (Carroll Q.B. 2018, Dance et al. 2014, Spahn M. 2013, Sequeiros et al. 2017)

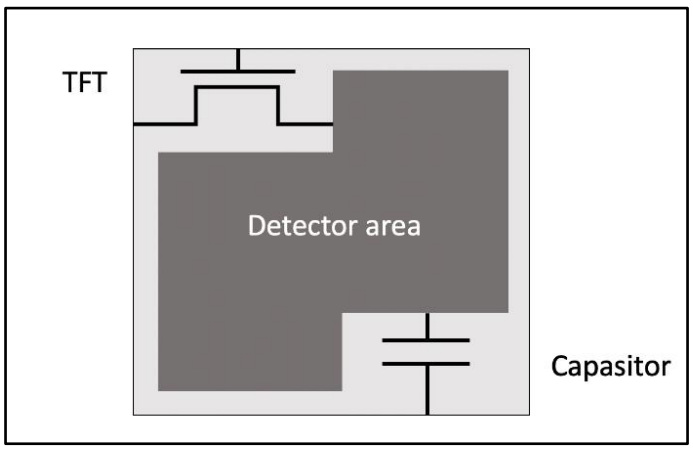


***Figure 11.*** *Top view of the detector element's overall structure. (Figure drawn based on Carroll Q.B. 2018, Dance et al. 2014 and Kabir M.Z. & Kasap S. 2017)*

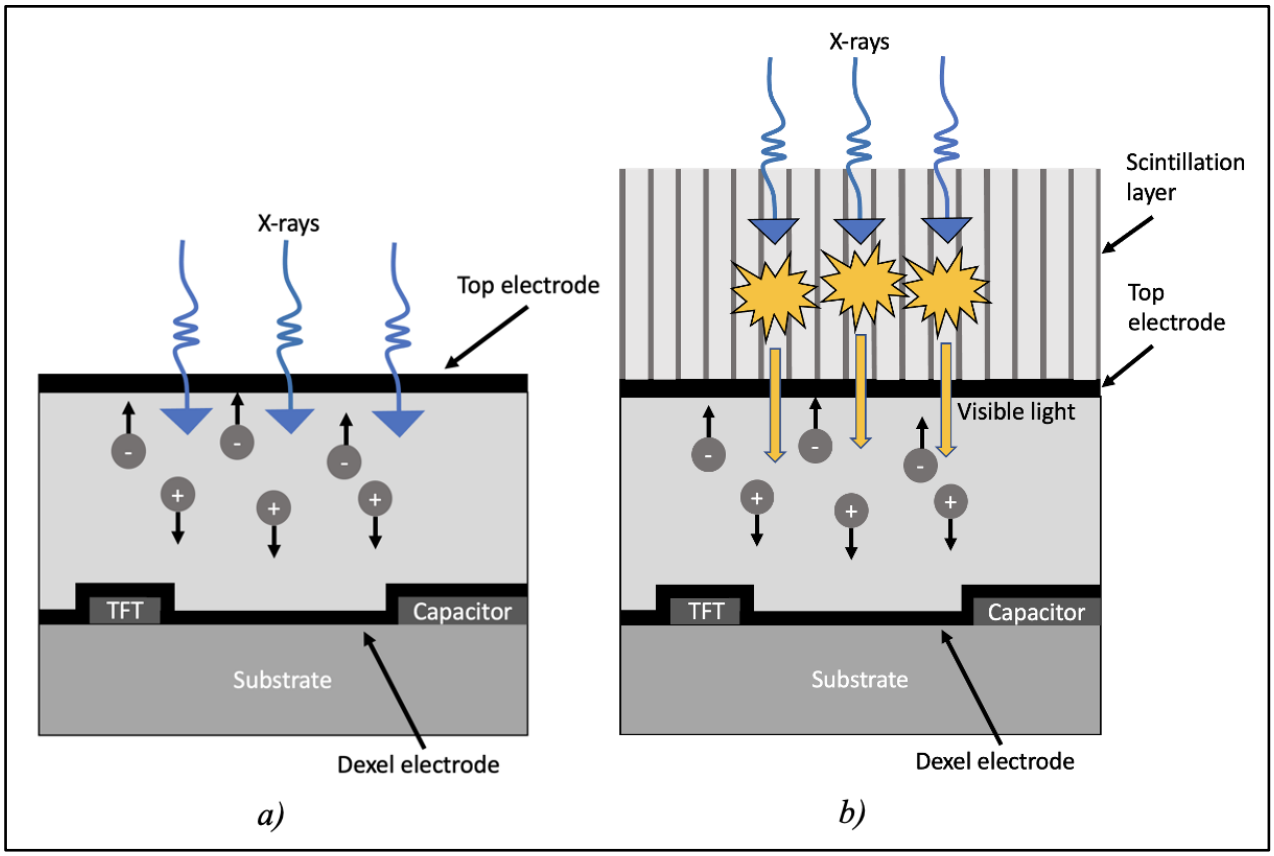


***Figure 12.*** *a) Cross-section view of the direct conversion dexel. b) Cross-section view of the indirect conversion dexel. (Figures drawn based on Q.B. 2018 and Kabir M.Z. & Kasap S. 2017)*

## 3. Radiation protection

In Finland the use of ionizing radiation is regulated by the law. STUK monitors that this law and the guidelines related to it are obeyed. Radiation law is based on the principles and recommendations given by the International Commission on Radiological Protection (ICRP), which was founded on 1928. (STUK 2004)

Main method for controlling the use of ionizing radiation is a licence procedure of which STUK is in charge in Finland. To receive the licence the use of radiation needs to fulfil three basic principles. These are: 1) justification principle, 2) optimization principle and 3) diagnostic reference level principle, of which the second is often referred to as "ALARA" principle based on sentence "As low as reasonably achievable".

These principles state respectively that: benefit of the experiment needs to outweigh the harm that possibly follows it, the experiment needs to be optimized so that the radiation dose received by patient is minimized and finally the dose received by any person participating the experiment may not exceed diagnostic reference levels set by the regulations. In addition to fulfilling these three principles the

licence applicant needs to reliable show in the application that all necessary actions have been done to ensure safe use of the radiation. (Jantunen H. et al. 2006, STUK 2004, Sequeiros et al. 2017)

After admitting licence STUK monitors the use of radiation by auditing location of the radiation usage. First audit is done before deployment of the imaging system and after that every 3 to 5 years depending on the type and the extent of usage. Practitioner of the radiation usage is for their part obligated to ensure safety of the radiation workers by fulfilling the actions listed on the STUK regulation ST 1.6. This regulation states for instance that radiation exposure of workers needs to be monitored and if necessary a personal dose surveillance needs to be conducted. (STUK 2004)

### *3.1 Monitoring radiation dose of workers*

All employees whose annual radiation dose can surpass 1 mSv are allocated as radiation workers. Employer is obligated by the law to arrange a dose surveillance to all radiation workers. Depending on the possible annual dose radiation workers are divided into two groups, A and B. Those employees whose annual effective dose can surpass 6 mSv, eye lens annual dose can surpass 15 mSv or skin, hand, arm, feet or ankle annual dose can surpass 150 mSv are allocated into group A. Other radiation workers belong to group B. (Finlex 2020a)

It is mandatory to arrange a personal dose surveillance to all radiation workers of the group A. This is done by an approved dose measurement service provider and the surveillance is implemented by wearing a personal dosimeter, which is read monthly. Measurement results are delivered to the STUK, which saves then into the dose register. For group B radiation workers, it is not mandatory to arrange personal dose surveillance, but in many cases it is appropriate. If it is arranged, reasonable interval for dosimeter reading is three months. (Finlex 2020a, Jantunen H. et al. 2006, Järvinen H. et al. 2018)

Finnish government regulation 1034/2018 sets limits for radiation doses received in work. These limits are presented in the *table 3*. (Finlex 2020a)

***Table 3.*** *Dose limits set for radiation workers by the government (Finlex 2020a).*

| ***Limited attribute*** | ***Dose limit*** |
|---|---|
| Annual effective dose | 20 mSv |
| Equivalent dose of eye lens during five consecutive years | 100 mSv<br>(without any annual dose reaching 50 mSv) |
| Annual equivalent dose of skin | 500 mSv |
| Annual equivalent dose of hands, arms, feet and ankles | 500 mSv |

*3.1.1 Dose variables*

When the ionizing radiation passes through the human body, part of its energy is absorbed by the tissues. The amount of absorbed energy is quantified by the absorbed dose *D*, that is gotten as a quotient of the absorbed energy (*E*) and the mass (*m*) of the object:

$$D = \frac{E}{m}. \qquad [3]$$

Unit of the absorbed dose is gray (Gy) according to SI unit system. (Sequeiros et al. 2017, Statkiewicz et al. 2018)

Dose area product (DAP) means a multiplication of dose (*D*) and area (*A*), and usually it is presented in unit mGy·cm$^2$ or Gy·cm$^2$. Many X-ray based imaging systems include DAP-meter, to enable evaluation of the patient dose. As DAP is practically independent of the distance from the X-ray tube focus, the measured DAP-value can be used as an estimate of DAP on the patient's skin. (Järvinen et al. 2018)

The biological effects caused by the ionizing radiation are dependent on the radiation type and the radiosensitivity of the affected organ. Respectively the equivalent ($H_T$) and the effective doses (*E*) take into account these factors and are used to evaluate biological effects of the radiation. The equivalent dose is gotten as a multiplication of dose (*D*) and radiation type weighting factor ($w_R$):

$$H_T = w_R D, \qquad [4]$$

From which the effective dose is gotten as a sum of the tissue sensitivity weighted equivalent doses:

$$E = \sum_T w_T H_T = \sum_T w_T \sum w_R D_{T,R}, \qquad [5]$$

where $w_R$ is a tissue weighting factor. Unit of both the equivalent and the effective dose is Sievert (Sv). Measured DAP-values can be used to estimate effective doses gotten by the patient. This is done by using published conversion factors. However notable uncertainties are related to this method. (Järvinen et al. 2018, Sequeiros et al. 2017, Statkiewicz et al. 2018)

On the dose surveillance of the staff, a quantity of personal dose equivalent $H_p(d)$ is used. It is defined as a dose equivalent on the depth d in soft tissue and can be measured with a dosimeter, which detector area is covered with an appropriate thickness of tissue equivalent. Values of the $H_p(10)$, $H_p(0,07)$ and $H_p(3)$ estimate respectively the whole body's effective dose, skins local equivalent dose and eye lens equivalent dose. (Arshak K. & Korostynska O. 2006, Järvinen et al. 2018)

*3.1.2 Dosimeters*

A radiation worker belonging to group A should wear a personal dosimeter at all times while working, i.e. when exposure to the radiation is possible. The dosimeter should be positioned so that it is perpendicular to the direction of the incoming radiation and so that it is not behind any body parts or protective shields. A good and commonly used place is attached to the thyroid shield the detector side of the dosimeter facing outwards (*Figure 13*). Another common place is the breast pocket. Today four types of personal dosimeters are commonly used. These include optically stimulated luminescence (OSL) dosimeters, thermoluminescent dosimeters (TLD), pocket ionization chambers and digital ionization dosimeters. In the next chapters the operation principles of these are presented. (Järvinen et al. 2018, Statkiewicz Sherer et al. 2018)


***Figure 13.*** *A personal dosimeter attached to a thyroid shield. When shield is used, it should be confirmed that the detector side of the dosimeter is facing outwards.*

OSL dosimeter consist of a layer of crystalline detection material on top of which are three filters positioned and one filter free area. Commonly used filter materials are aluminium, copper and tin. During radiation exposure electrons are released from atomic orbitals of the detection material and these electrons are trapped in a metastable state similar to CR detector plates. The reading of the dosimeter is done also in a same manner as in the CR by scanning the detector with a laser. This causes electrons to fall back to the atomic orbitals and energy is simultaneously released as a

luminescence. The amount of the luminescence behind filters varies depending on the attenuation of the filter material. This enables estimation of the half-value layer, from which the energy range of the original radiation can be derived. The reader which is used for the luminescence detection is based on a photomultiplier tube, which detects light, converts it into a electrical form and amplifies the signal. (Carroll Q.B. 2018, Statkiewicz Sherer et al. 2018)

TLD's operating principle and overall structure resembles the OSL dosimeter described in the previous chapter. Differing from OLS, the reading of dosimeter happens through a special heating process. When the detector material is heated, trapped electrons energies increase in a manner that allows them to return to the atomic orbitals via conduction band. When electrons bond to orbitals, energy is realised as a luminescence. The intensity of the luminescence is proportional to the intensity of the exposure radiation and to the attenuation of the possible filter positioned in front of the detector. (Carroll Q.B. 2018, Statkiewicz Sherer et al. 2018)

Pocket ionization chamber (pocket dosimeter) is a gas-filled detector. The external appearance of the pocket dosimeter resembles that of a ballpoint pen, and it can be easily attached to a breast pocket of a jacket with a clip included to it. Inside structure of the dosimeter consists of a gas filled cylindrical chamber and two electrodes. The first electrode is a positively charged pin like central electrode, which by its name is positioned on the centre of the cylinder. Second electrode is depending on the dosimeter model either negatively or positively charged. If we consider a self-reading model, then the second electrode is positively charged, and it is positioned on one side of the cylinder wall. When exposed to ionizing radiation, electrons are released from the gas inside dosimeter. Released electrons are attracted to positively charged central electrode and so charge of the central electrode is decreased. This causes the central electrode to move toward the wall electrode. This movement can be viewed through the scaled window positioned on the end of self-reading dosimeter. (Carroll Q.B. 2018, Statkiewicz Sherer 2018)

Digital ionization dosimeters are quite new devices on the personal dosimetry. Their structure includes a small ionization chamber and a semiconductor component. When the dosimeter is exposed to the ionizing radiation, a small electrical charge is produced in the ionization chamber. This charge is delivered and stored in the semiconductor component. The dose can be read by connecting the dosimeter into a computer through an USB-port. (Statkiewicz Sherer 2018)

### *3.2 Radiation protection for medical professionals*

Radiation workers' principal source of the radiation exposure is the scattered radiation (Rodas N.L. & Padoy N. 2015). It is caused by any object in the path of the X-ray beam (Jentzsch T. et al. 2015). Chida et al. (2011) discovered in their research by using a pin hole camera that the main sources of scattered radiation during interventional radiology are the patient, the patient table and the cover of the X-ray beam collimating device. Although the cover of the collimating device is made of low an attenuation material, the scattered radiation arising from it reaches significantly high level, because of its close position to the X-ray source. However, the level of scattered radiation arising from the patient is much greater.

There are several situations and job descriptions in which the healthcare worker can be exposed to the ionizing radiation. The biggest dose values received by healthcare personnel using X-rays have been reported among physicians conducting interventional procedures. Other common situation is holding the patient during imaging. In these situations, it is vital that all possible ways are used to minimize the dose received by the staff. IAEA has made two posters that summarize methods for radiation protection of the patients and the staff during fluoroscopy (IAEA 2020b and 2020c). Guidelines of these posters can be mostly applied in other X-ray based imaging modalities as well. Next chapters will discuss in more detail of these methods. (Jantunen H. et al. 2006, Roguin et al. 2013, Statkiewicz Sherer et al. 2018)

#### *3.2.1 Minimizing patient dose*

As the amount of scattered radiation and the patient dose are proportional, decreasing patient dose also lowers the dose received by the personnel (Miller D.L. et al. 2009). For this reason it is essential to optimize imaging parameters and positioning. Regarding patient positioning there are two main methods to ensure the best image quality at lowest dose. These are placing the patient as far from the X-ray tube as possible and as close to the image receptor as possible. This setup will minimize patient's skin dose and maximize the radiation detected by the image receptor. (Bartal G. et al 2013, Dance et al. 2014, IAEA 2020a)

In addition to positioning, also imaging equipment parameter optimization is vital to minimizing the patient dose and the scatter. Part of these parameters are experiment dependent. However, some parameter recommendations can be given in general level and they should be utilized always. These

include: use tight collimation and avoid magnification unless it's absolutely necessary. For fluoroscopy it can be additionally stated that fluoroscopy time should be minimized, lowest sufficient dose rate and pulse rate should be used, and last image hold option should be exploit. (Bartal G. et al. 2014, Dance et al. 2014, Miller D.L. et al. 2010)

As mentioned in chapter 1 (Ionizing radiation), children's bodies include a lot of highly mitotic tissues, which make them more sensitive to ionizing radiation compared to the adults. In addition, special characteristics of children's body complicate protection of these risk tissues from the radiation. In general bodies of young children are shorter and wider compared to adults. For this reason, when taking X-ray images larger proportion of the body is exposed to the radiation. Also, the distribution of risk tissues is more widespread in children, which further complicates protecting them. When these special characteristics are combined with the fact that children's lifetime expectancy is longer and so time for stochastic effects to emerge is also long, it is evident that minimizing the radiation dose in the pediatric X-ray imaging is critical. (Alzen G. & Benz-Bohm G. 2011)

All in this chapter previously listed dose reduction methods apply to children as well. However, there are some special techniques to reduce exposure in pediatric imaging. Firstly, a list of indications, containing imaging type and number of projections related to it, should be generated. Secondly, manual imaging should be used instead of an automatic. Thirdly, use of grid is not advisable for small children. Additionally, it can be stated for pediatric imaging: use gonad, thyroid, ovary and breast shields (also recommended for adults, but essential for children), use maximal value of the recommended tube voltage and use additional filtration. (Alzen G. & Benz-Bohm G. 2011, IAEA 2012)

### *3.2.2 Minimizing staff dose*

So called time-distance-shielding (TDS) principle forms the foundation of radiation protection of the personnel. It denotes that the exposure time should be minimized, distance to the radiation source should be maximized and an appropriate shielding should be used. Following chapters discuss more of these methods. (Dance et al. 2014, Ehrlich R.A. & Coakes D.M. 2017, IAEA 2020c, Statkiewicz Sherer et al. 2018)

The amount of radiation exposure of the personnel is directly proportional to the time spent in the radiation field. For this reason, it is essential to limit exposure time to minimum. Especially during

fluoroscopic procedures this is vital, as these procedures can be lengthy. Fluoroscopic devices are as default equipped with a 5-minute alarm, that reminds the operator of the exposure cumulation. (Statkiewicz Sherer et al. 2018)

According to the inverse square law (*Equation 6*) the intensity of radiation (*I*) is inversely proportional to the square of the distance (*d*) from radiation origin. Therefore, increasing distance to the radiation source decreases rapidly the amount of the exposure. For example, when the distance to the source is doubled the dose received drops to one fourth. Consequently, it is important to maximize the distance to the radiation source. (Dance et al. 2014, Statkiewicz Sherer et al. 2018)

$$\frac{I_1}{I_2} = \frac{(d_2)^2}{(d_1)^2}, \qquad [6]$$

where $I_1$ and $I_2$ correspond to radiation intensity on the distances $d_1$ and $d_2$ respectively. (Statkiewicz Sherer et al. 2018)

If healthcare personnel are forced to stay in the examination or the operation room during the radiation exposure, an appropriate shielding should be used whenever it is practically possible. There are three kinds of shields: personal, stationary/mobile and structural. A lead apron and a thyroid shield comprise the basis of the personal shielding (*Figure 14 a*). The protection capability of these must be at minimum equivalent to 0.25 mm of lead. The popular models of body protection are a jacket or a combination of a vest and a skirt. In both of these the front parts overlap making the protection correspond to 0.5 mm lead equivalent. Additionally, to the apron and the thyroid shield, either protective leaded eyeglasses (*Figure 14 b*) or a ceiling mounted shield is recommended (*Figure 14 c*). The latter of these provides also protection for the head and the neck and can be hence preferable choice if applicable. It should be noted that the effectiveness of the ceiling mounted shield is highly depended on the correct positioning of the shield. (Dance et al. 2014, Miller D.L. et al. 2009, STUK 2018)

The stationary and the mobile shields can be used to further improve the safety of the radiation workers during the imaging. Especially these are exploited during interventional procedures. Commonly used stationary shields include the ceiling mounted shield, that was mentioned in the previous chapter, and a radiation protective lamella curtain (*Figure 14 c*), that is attached to the operation table. Table mounted lamella curtain protects personnel's lower body parts from the

scattered radiation that is oriented downwards. In addition to these, stationary or mobile radiation protective walls (*Figure 14 d*) can be used for example by an anaesthesia personnel during the operation. (STUK 2018)

Structural shields include ceiling, walls, floor, windows and doors of the imaging room. Rooms inside radiology department are divided into a controlled area, a surveillance area and an uncontrolled area based on the amount of the possible exposure to ionizing radiation in them. The controlled area and the surveillance area are primarily occupied only by the radiation workers. The uncontrolled area comprises of the rooms and hallways located outside the actual imaging rooms. Annual effective dose limits for controlled and uncontrolled areas are 6 mSv and 0,3 mSv respectively and the building structures need to be constructed so that these limits are not surpassed. (Carroll Q.B. 2018, Finlex 2020b, STUK 2011)


***Figure 14.*** *Examples of radiation protective shields. a) A body protection shield that consists of a vest and a skirt accompanied with a thyroid shield. b) A protective leaded eyeglasses. c) A ceiling mounted shield and an operation table mounted radiation protective lamella curtain. d) A mobile radiation protective wall.*

In addition to time, distance and shielding, there are several other methods to increase the safety in the radiation work. These include training and correct positioning of the staff and the X-ray source. Appropriate training for conducting radiation work is essential for both the patient and the staff safety. For this reason, organizing a proper training and a regularly conducted re-training for all radiation

workers is registered in the Finnish radiation law as a responsibility of the practitioner of radiation usage. Based on the EU directive 2013/59/EURATOM similar training practices are required in all EU countries. (Bartal G. et al 2014, Eur-lex 2020, Finlex 2020b, Jentzsch T. et al. 2015, Miller D.L. et al 2009)

Positioning oneself in a low scatter area is an effective way to lower the exposure dose (Ardiatna W. et al. 2020). Therefore, providing a knowledge of the distribution of the scattered radiation inside the operation or the examination room is invaluable part of the training (Wagner M. et al. 2012). This is done generally using simulations (Rodas N.L. & Padoy N. 2015, Süncksen M. et al. 2020, Wagner M. et al. 2012) or multi dosimeter measurements (Nakamura T. et al. 2020, Nowak M. et al. 2020).

The positioning of the X-ray source determines the spatial distribution of the scatter radiation fields inside the examination or operation room. Consequently, correct positioning of the X-ray source with respect to personnel should be considered. If the C-arm is used in a lateral position, personnel should stand on the detector side of the operating table. This minimizes their exposure as the intensity of the scattered radiation field is highest on the side where the X-ray beam enters patient. Accordingly, the X-ray tube should be positioned under the operation table when the C-arm is used in a vertical position. This way most of the scattered radiation is directed towards the floor. (IAEA 2020c, Jentzsch T. et al. 2015)

# Methods

In this study a semiconductor dosimeter system (Raysafe i2, Unfors Raysafe AB, Sweden) was used to collect the dose rate values of the scattered X-ray radiation. The systems original purpose is to monitor the personal dose values of the healthcare personnel and it's operational measurement quantity is $H_p(10)$, i.e. personal dose equivalent at tissue depth of 10 mm. System consists of pocket-sized semiconductor dosimeters, a 10.4-inch touch panel (*Figure 15*) and a Dose Manager software. Each dosimeter's dose values can be viewed in real-time from the touch panel during measurement and afterwards from the Dose Manager software. Dose Manager software presents the accumulated dose and dose rates as a function of time. (Unfors Raysafe AB 2020)


***Figure 15.*** *Semiconductor dosimeters and a touchpanel of Raysafe i2 measurement system. (Image retrieved from web site www.raysafe.com)*

In this research an ATOM dosimetry verification phantom 701/C was used as a scattering object. It is an adult male phantom, that comprises of 25 mm thick sections. This anthropomorphic phantom includes tissue equivalent structures. *Figures 16 a)* and *b)* present images of the phantom taken during standing and supine radiography.

Three dosimeters were selected for measurements and they were attached to an infusion stand on three heights. Installation heights varied from one measurement setup to other. The middle one of dosimeters was positioned close to the height where most of the scattering occurred, i.e. close to a centre of a radiation beam entry point to the phantom. *Figure 16* shows the installation heights of the centremost dosimeters when phantom was placed horizontally and vertically. The other two dosimeters were positioned +/- 35 cm or +/- 30 cm from the middle one depending on the

measurement setup. Installation heights of the upper and the lower dosimeter were selected quite close to the centremost, because of the dosimeter's angular dependence, i.e. accuracy of the dosemeter decreases when angle of coming radiation increases. In addition, the posture and the position of possible healthcare personnel or other assisting person in room during imaging was considered, when selecting dosimeter installation heights. For example, during thorax imaging this person could be standing next to the patient and during urological operation the physician would be sitting on the end of patient table. The upper dosimeter position was selected when possible so that it would be close to height of eyes of healthcare personnel. The actual installation heights for each room are presented on the *table 4*.

Measurements were done in three rooms using four different imaging setups. These rooms were Oulu university hospital's children's X-ray examination room (L6 R39), surgical operating room (K6 293) and general X-ray examination room (N4 113). In the first room the stationary imaging equipment of this room was used to acquire standing thorax PA radiographs and supine pelvis AP radiographs. On the last two rooms two different mobile imaging devices were used for fluoroscopy and to acquire supine thorax AP radiographs, respectively. *Figure 17* presents images of used measuring setups, and *tables 4 and 5* present the details of the setups and the imaging parameters, respectively.


***Figure 16.*** *a) Phantom positioned horizontally. Installation height of the centremost dosimeter marked with red arrow, b) Phantom positioned vertically. Installation height of the centremost dosimeter marked with red arrow.*

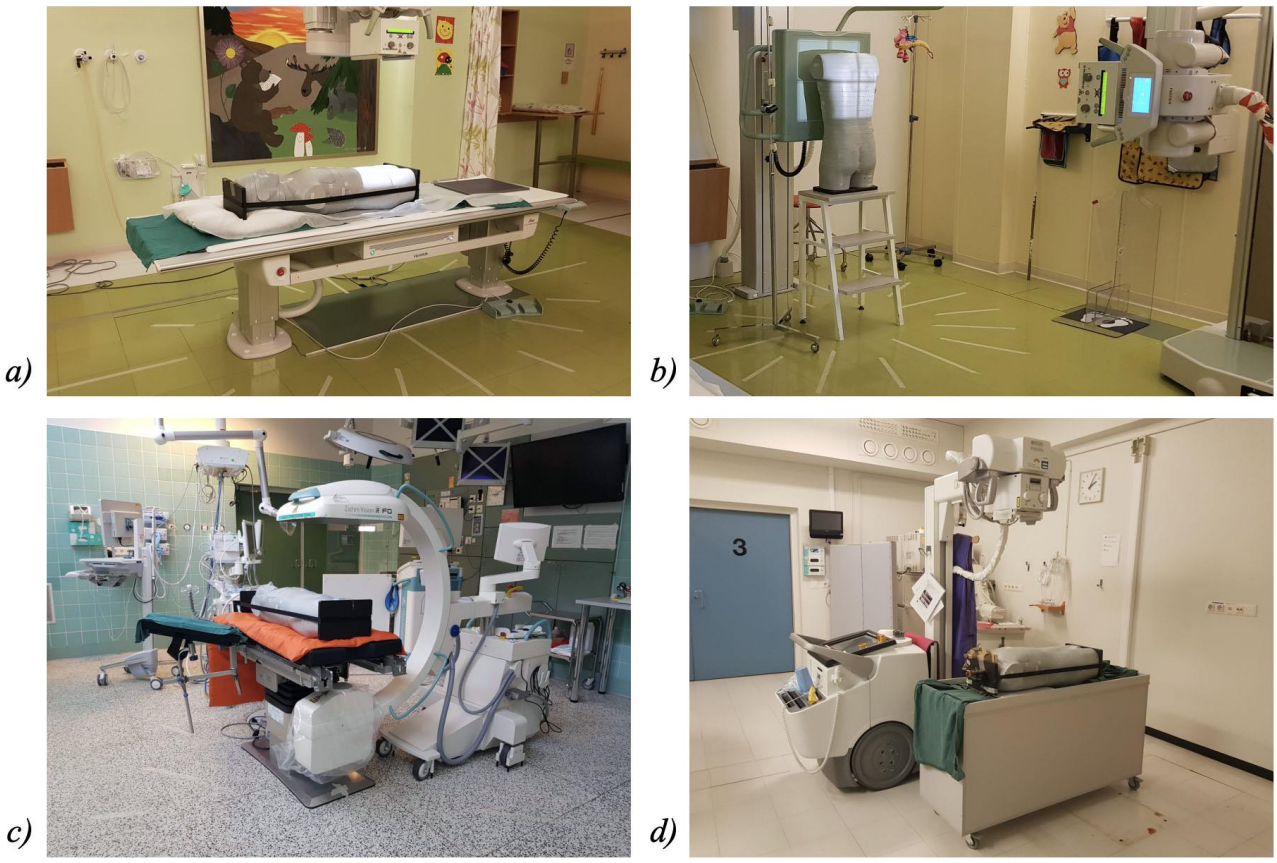


***Figure 17.*** *Measuring setups used for: a) supine radiography in the children's X-ray imaging room, b) standing radiography in the children's X-ray imaging room, c) mobile fluoroscopy in the operating room and d) mobile supine radiography in the general X-ray examination room.*

***Table 4.*** *Imaging related parameters: room, imaging device, posture, patient group, imaging program, used radiation protection and dosimeter installation heights.*

| **Room, imaging device** | **Posture** | **Patient group** | **Imaging program** | **Radiation protection** | **Dosimeter installation hights (cm)** | **Measurement distances (m)** |
|---|---|---|---|---|---|---|
| L6 R39, Fujifilm (Children x-ray examination room) | Standing | Child (50kg) | Thorax PA child 50kg, no grid | - | 105, 135, 165 | 0.5, 1, 1.5, 2, 2.5, 3 |
| L6 R39, Fujifilm | Standing | Adult | Thorax PA | - | 105, 135, 165 | 0.5, 1, 1.5, 2, 2.5, 3 |
| L6 R39, Fujifilm | Standing | Adult | Thorax PA | Pelvic shield | 105, 135, 165 | 0.5, 1, 1.5, 2, 2.5, 3 |
| L6 R39, Fujifilm | Standing | Adult | Thorax LAT | - | 105, 135, 165 | 0.5, 1, 1.5, 2, 2.5, 3 |
| L6 R39, Fujifilm | Supine | Child (50kg) | Pelvis AP child 50kg | - | 50, 80, 110 | 0.5, 1, 1.5, 2, 2.5, 3 |
| L6 R39, Fujifilm | Supine | Adult | Pelvis AP | - | 50, 80, 110 | 0.5, 1, 1.5, 2, 2.5, 3 |

| | | | | | | |
|---|---|---|---|---|---|---|
| L6 R39, Fujifilm | Supine | Adult | Pelvis AP | Radiation protection blanket | 50, 80, 110 | 0.5, 1, 1.5, 2, 2.5, 3 |
| K6 293, Ziehm Vision RFD (Operating room) | Supine | Adult | Ureteral stent insertion (KBV02) | - | 70, 105, 140 | 0.5, 1, 1.5, 2, 2.5 |
| K6 293, Ziehm Vision RFD | Supine | Adult | Ureteral stent insertion (KBV02) | Lamella radiation protection curtain | 70, 105, 140 | 0.5, 1, 1.5, 2, 2.5 |
| N4 113, Philips SkyFlow (X-ray examination room) | Supine | Adult | Thorax AP with grid adult 60-80kg | - | 50, 85, 120 | 0.7, 1, 1.3, 1.6, 1.9 |

***Table 5.*** *Imaging modality and parameters used in each imaging program.*

| **Imaging program** | **Imaging modality** | **Tube voltage, exposure (for fluoroscopy tube current and pulse rate are presented)** |
|---|---|---|
| Thorax PA child 50 kg | DR | 130 kVp, 2 mAs |
| Thorax PA adult (L6 R39) | DR | 125 kVp, 1.75 mAs |
| Thorax lateral adult | DR | 125 kVp, 8.5 mAs |
| Pelvis AP child 50 kg | CR | 71 kVp, 12.5 mAs |
| Pelvis AP adult | CR | 81 kVp, 16.5 mAs |
| Ureteral stent insertion (KBV02) | Mobile DR fluoroscopy | 66 kVp, 9.3 mA, 25.5 pulses/s |
| Thorax AP adult 60-80kg (N4 113) | Mobile DR | 125 kVp, 0.7 mAs |

In all imaging setups the measurements were done clockwise around the scattering object. The angular difference between adjacent measurement points was 22.5°. Measurement distances were 0.5 m, 1 m, 1.5 m, 2 m, 2.5 m and 3 m from the scatter origin, except in the room N4 113 where measurement distances were 0.7 m, 1 m, 1.3 m, 1.6 m and 1.9 m (*Table 4*). *Figures 18* and *19* illustrate the measurement points with respect to the scatter source, i.e. phantom, and with respect to the room layout. Measurement was done in all points where it was possible with the used measuring system. For example, the room's fixed furniture, the imaging equipment and the dosimeter holder prevented measurements in some points. In addition, in standing thorax PA radiography the primary beam area was excluded from the measurements, as putting the dosimeter holder (infusion stand) in primary beam would affect the imaging parameters due to the automatic exposure control.

Measurement information was collected on a log sheet during measurements. After each measurement the point of time in minute accuracy was written down. This way it was possible to identify each measurement from the Dose Manager program's dose graphs later on. Additionally, measurement date, imaging device, measurement distance from scatter origin, imaging program, used radiation protection, position of scattering object in room and room overall measures were written down. Some of these were needed for the scatter map implementation and some for the result evaluation. *Table 4* presents those that are essential for the result evaluation. To be able to induce maximum scatter in each imaging setup, no collimation of the radiation field was used.

After measurements were finished, the $H_p(10)$ personal dose equivalent values were read from the Dose Manager software. Each dose value and its corresponding x- and y-coordinates were written on a Matlab file. Altogether 30 files were gathered in this manner, as there were 10 different imaging setups and in all these three dosemeters on three hights were used (*Table 4*). As the manufacturer does not recommend using dosimeters in the primary beam, a scattered radiation dose rate value for the phantom's centre point in the primary beam was evaluated by extrapolating the existing data. Extrapolated values were added on the measuring files. This was done to prevent any misleading lower dose curves to be drawn on the position of phantom by the Matlab program described in the next chapter.

A ready-made Matlab program called X-ray scattering tool (Saarakkala et al. 2007) was used to generate maps of scattered radiation. Layout of each room was downloaded on the program and the scale of layout was defined by selecting origin and specifying coordinates of one known point. After this, one of dose rate files were downloaded on the program and the scatter map was drawn.

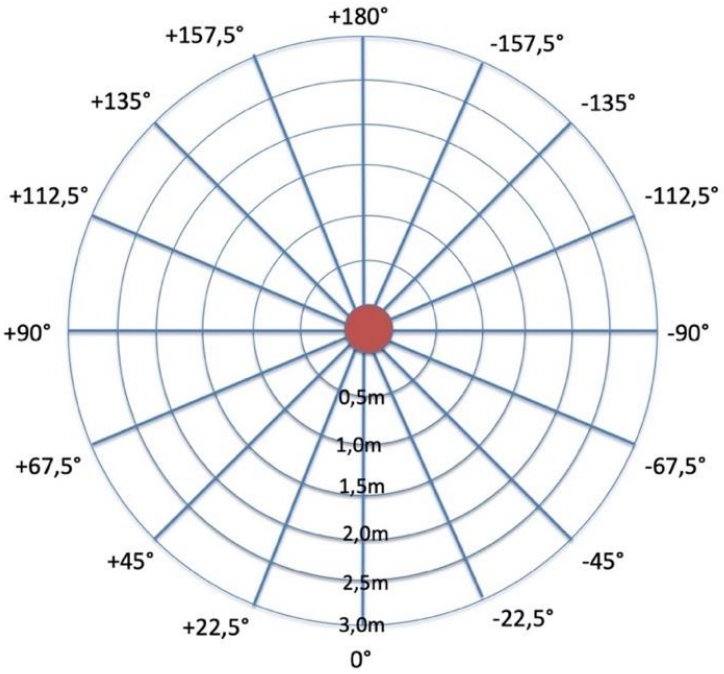


***Figure 18.*** *Specification of measurement points used in rooms L6 R39 and K6 293. In N4 113 specification of the measurement points was done otherwise similarly, but the measurement distances were 0.7, 1, 1.3, 1.6 and 1.9m from the scatter origin.*

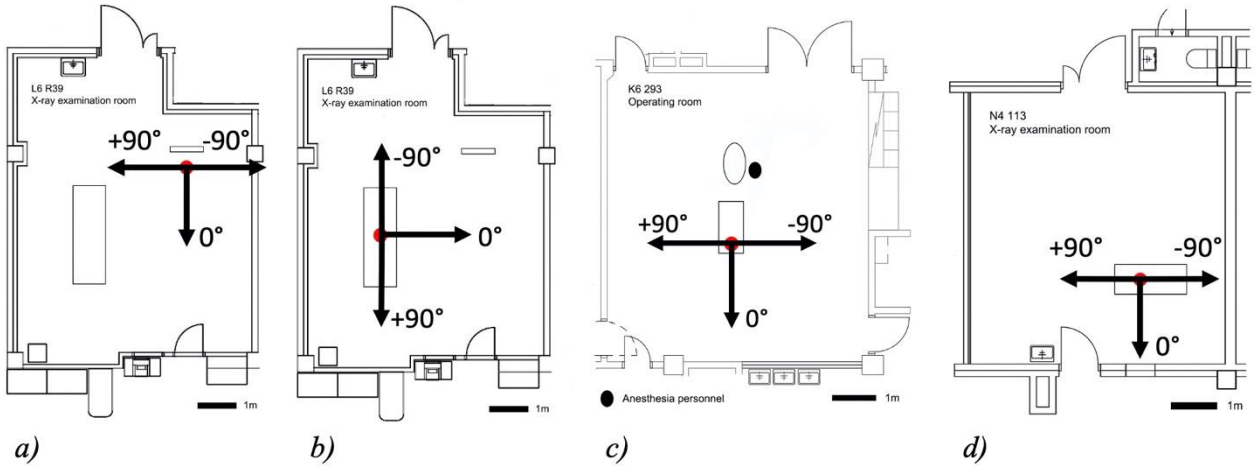


***Figure 19.*** *Measurement point orientation with respect to the room layout for each measurement setup. a) L6 R39 standing position, b) L6 R39 supine position, c) K6 293 and d) N4 113.*

# Results

## 1. Presentation of the implemented scattered radiation maps

Implemented scattered radiation maps are presented in the following figures 20 - 29. Each figure presents all three maps which were acquired during the same measurement at different heights. The figures present maps in order presented in the *table 6*. Next chapters go through these figures and characterize each map.

***Table 6.*** *Details of the scattered radiation map figures.*

| Figure | Patient group | Imaging equipment | Imaging program | Phantom position (shield) |
|---|---|---|---|---|
| 20 | Adult | Stationary DR | Thorax PA | Standing |
| 21 | Adult | Stationary DR | Thorax PA | Standing (pelvic shield) |
| 22 | Adult | Stationary DR | Thorax Lateral | Standing |
| 23 | Child 50kg | Stationary DR | Thorax PA | Standing |
| 34 | Adult | Stationary CR | Pelvis AP | Supine |
| 25 | Adult | Stationary CR | Pelvis AP | Supine (radiation protection blanket) |
| 26 | Child 50kg | Stationary CR | Pelvis AP | Supine |
| 27 | Adult | Mobile fluoroscope | Ureter stent installation | Supine |
| 28 | Adult | Mobile fluoroscope | Ureter stent installation | Supine (lamella radiation protection curtain) |
| 29 | Adult | Mobile DR | Thorax AP | Supine |

Thorax PA and lateral with stationary DR

*Figure 20* presents scatter maps acquired with stationary DR using adult's Thorax PA imaging program with the phantom placed in a standing position. In this figure the scattered radiation is presented at the heights of 105 cm, 135 cm and 165 cm. The most prominent feature of all three maps is, that the scattered radiation is strongly emphasized towards the X-ray tube (i.e. downwards on images). When comparing the dose rate values of these three maps, there isn't much difference, though dose rate values of the centre most dosimeter seem to be slightly higher than other two.

*Figure 21* presents scatter maps acquired with stationary DR by using adult's Thorax PA imaging program with the phantom placed in a standing position with a pelvic shield. In this figure the scattered radiation is presented at the heights of 105 cm, 135 cm and 165 cm. Features of these maps are equivalent to the maps described on the previous chapter and presented on *figure 20*.

*Figure 22* presents scatter maps acquired with stationary DR by using adult's Thorax Lateral imaging program with the phantom placed in standing position. In this figure the scattered radiation is presented at the heights of 105 cm, 135 cm and 165 cm. The most prominent feature of all three maps is, that the scattered radiation is very strongly emphasized towards the X-ray tube (i.e. downwards on images). When comparing the dose rate values of these three maps, the upper most dosimeter's values are lower than the other two dosimeters. When dose rate values of this figure are compared to *figure 20* (Thorax PA adult), it is evident that the scattered radiation is higher in Thorax lateral imaging.

*Figure 23* presents scatter maps acquired with stationary DR by using 50 kg child's Thorax PA imaging program with the phantom placed in standing position. In this figure the scattered radiation is presented at the heights of 105 cm, 135 cm and 165 cm. Features of these maps are equivalent to the maps presented on *figures 20* and *21*, which include scatter maps of adult's Thorax PA without a shield and with a pelvic shield.

If a person would be assisting during the standing Thorax PA or Lateral DR by holding or calming the patient, this person would most likely be positioned on the side of the patient. 0.5 m away from patient (red dot on the figures), in a way that she or he would not intersect the primary beam. In this situation the assisting person would be exposed to scattered radiation. *Table 7* comprises dose rates detected on the left side of the phantom at the height of 135cm at distance 0.5 during Thorax PA and lateral imaging. This table also includes cumulative equivalent dose values calculated based on exposure times gotten from DICOM images.

***Table 7.*** *Estimating dose of an assisting person during Thorax PA and Lateral DR. Table presents measured dose rates at the height of 135 cm at left side of patient at distance 0.5 meter, exposure times gotten from DICOM images and calculated cumulative $H_p(10)$ equivalent doses during imaging.*

| **Experiment** | **Dose rate at distance 0.5 m** | **Exposure time** | **Cumulative equivalent dose at distance 0.5 m** |
|---|---|---|---|
| Thorax PA adult | 1692 µSv/h | 11 ms | 5.17 nSv |
| Thorax Lateral adult | 6108 µSv/h | 28 ms | 47.5 nSv |

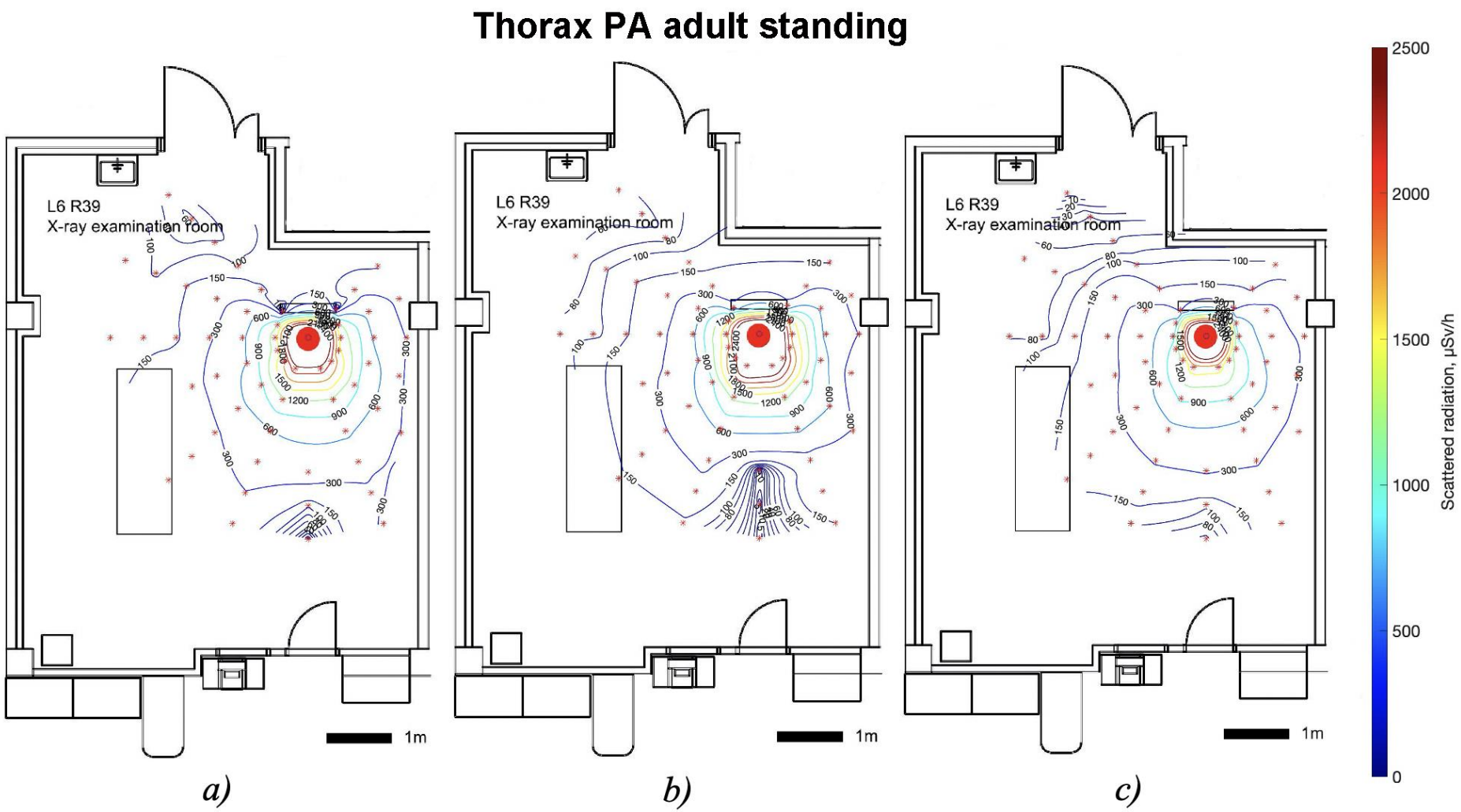


***Figure 20.*** *Scattered radiation maps acquired with stationary DR by using adult's Thorax PA imaging program with the phantom placed in standing position. Scattered radiation is presented for heights a) 105cm, b)135cm and 165cm.*

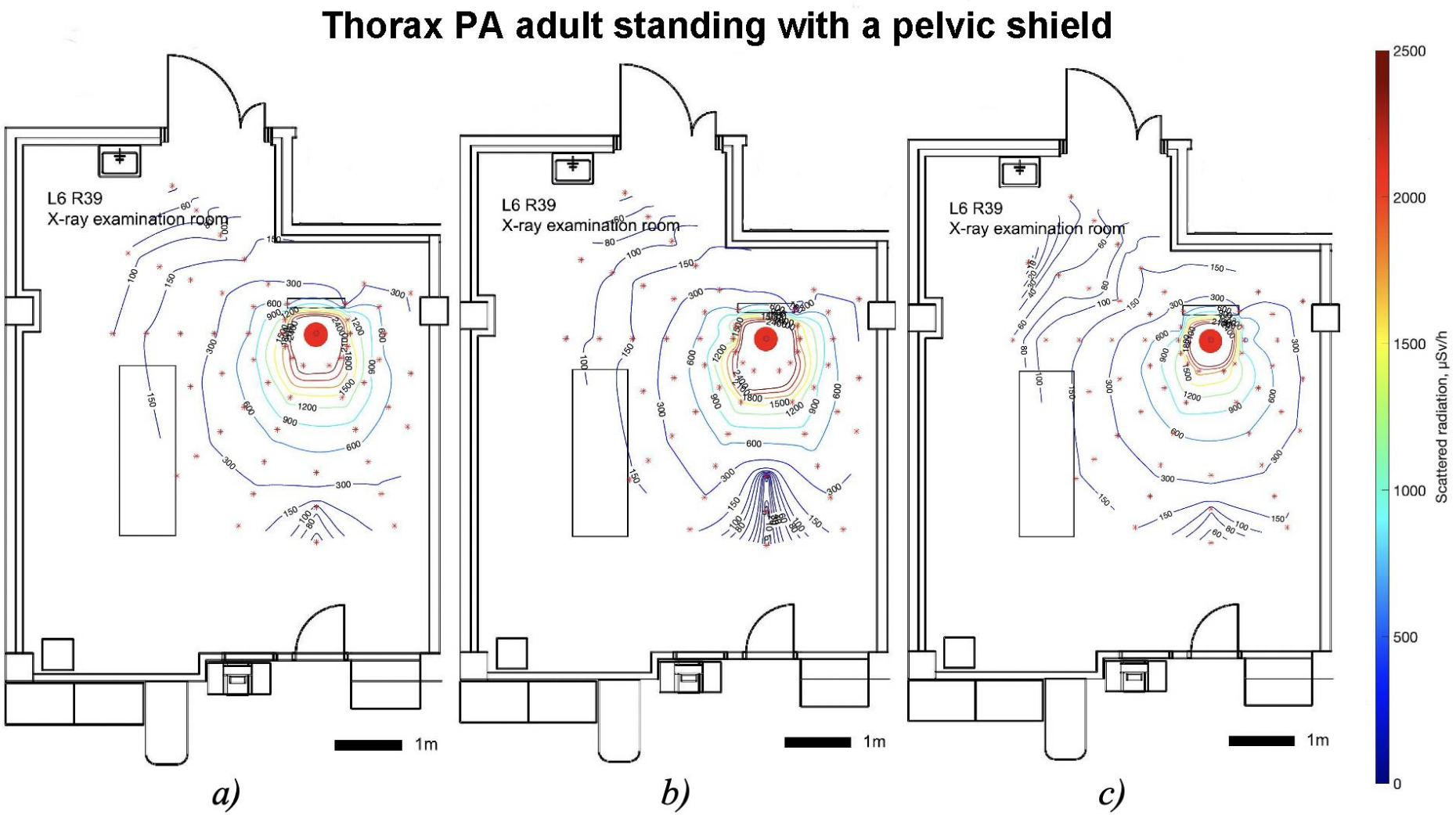


***Figure 21.*** *Scattered radiation maps acquired with stationary DR by using adult's Thorax PA imaging program with the phantom placed in standing position with a pelvic shield. Scattered radiation is presented for heights a) 105cm, b) 135cm and 165cm.*

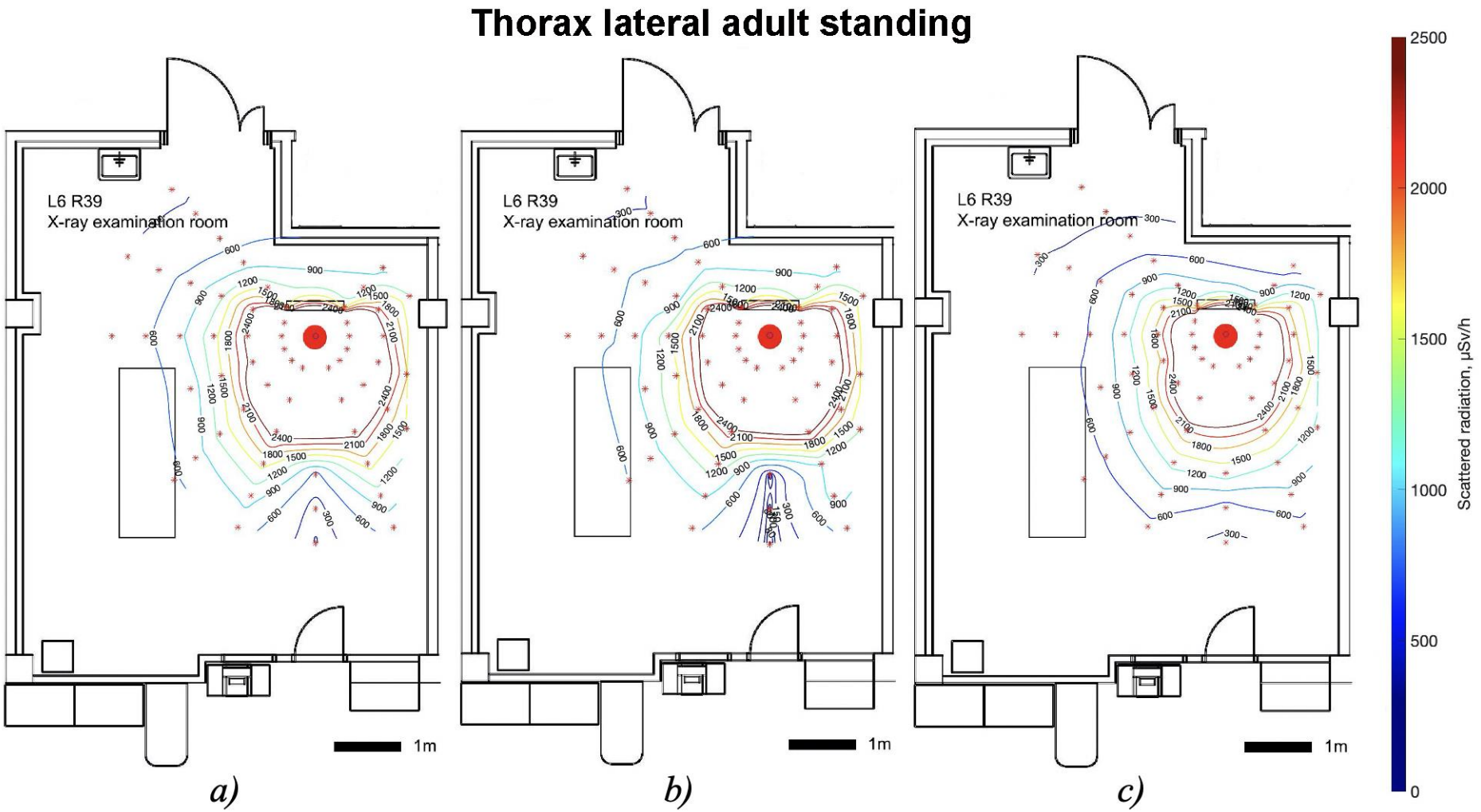


***Figure 22.*** *Scattered radiation maps acquired with stationary DR by using adult's Thorax Lateral imaging program with the phantom placed in standing position. Scattered radiation is presented for heights a) 105cm, b) 135cm and 165cm.*

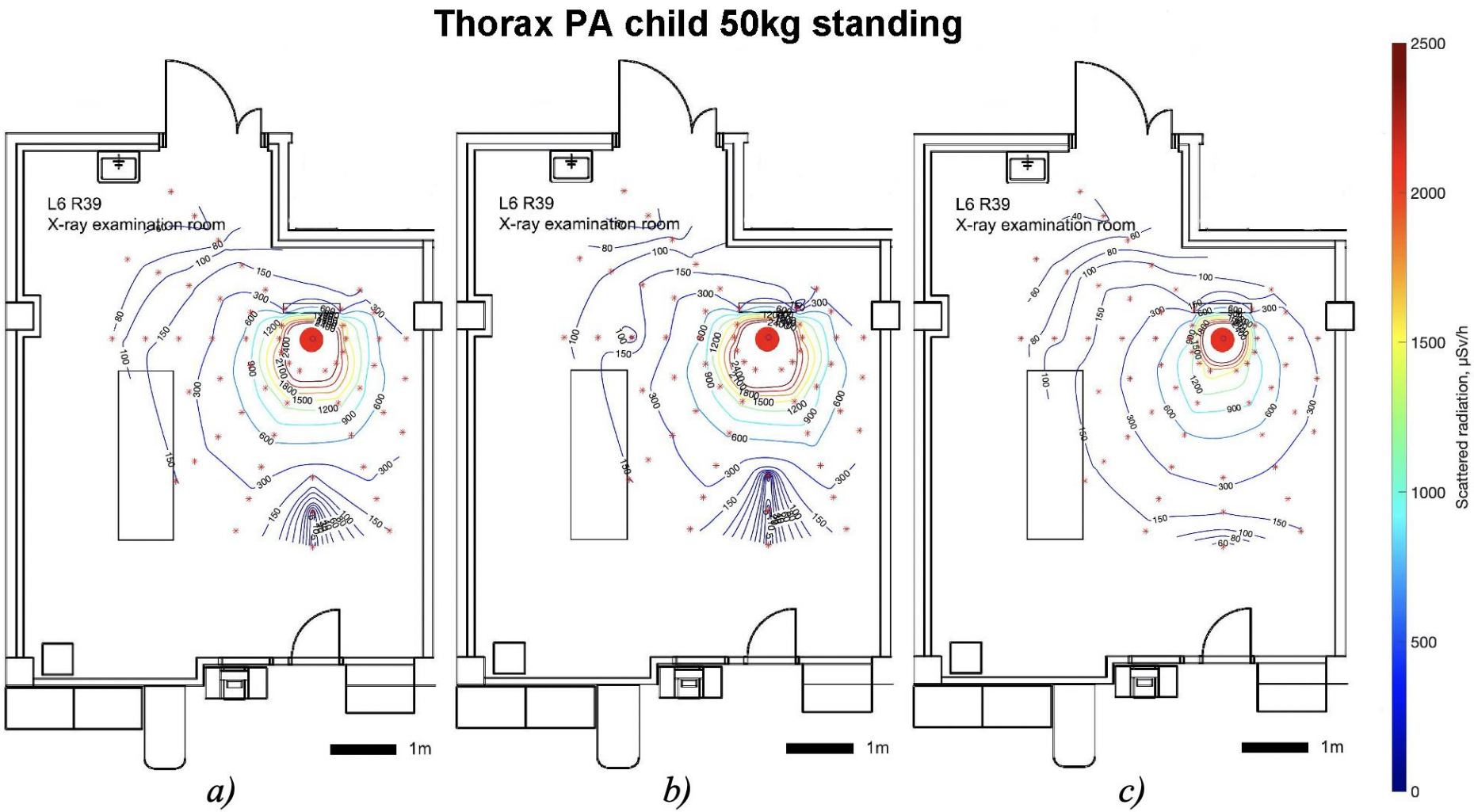


***Figure 23.*** *Scattered radiation maps acquired with stationary DR by using 50 kg child's Thorax PA imaging program with the phantom placed in standing position. Scattered radiation is presented for heights a) 105cm, b) 135cm and 165cm.*

Pelvis AP with stationary CR

*Figure 24* presents scatter maps acquired with a stationary CR using the adult's Pelvis AP imaging program with the phantom placed in a supine position. In this figure the scattered radiation is presented at the heights of 50 cm, 80 cm and 110 cm, of which the first is lower than the patient table surface. The most prominent features of the scatter maps at height of 80 cm and 110 cm are, that the scattered radiation is directed quite equally to all directions around the phantom and that dose rates of these maps are similar. The scattered radiation at the height 50 cm differs from the other two, and the map at this height is quite complex when both shape and dose rates are considered.

*Figure 25* presents scatter maps acquired with stationary CR by using the adult's Pelvis AP imaging program with the phantom placed in a supine position with a radiation protection blanket placed to cover the chest area. The chest is positioned on the lower part of the patient table in the images. In this figure the scattered radiation is presented at the heights of 50 cm, 80 cm and 110 cm. Features of these maps are equivalent to the maps described on the previous chapter and presented on the *figure 24.*

*Figure 26* presents scatter maps acquired with stationary CR by using 50 kg child's Pelvis AP imaging program with the phantom placed in supine position. In this figure the scattered radiation is presented at the heights of 50 cm, 80 cm and 110 cm. Features of these maps are equivalent to the maps presented on *figures 24* and *25*.

If a person was assisting during supine Pelvis AP CR by holding or calming the patient, this person could be positioned at the end of the patient table or at the side of the table. *Table 8* comprises dose rates detected at the height of 80cm at the upper end (on the figures) of the patient table and at the right side of table. Table also includes cumulative equivalent doses calculated from the dose rates based on the exposure times gotten from DICOM images.

***Table 8.*** *Estimating dose of an assisting person during Pelvis AP CR. Table presents measured dose rates at the height of 80 cm at the (figures) upper end of the patient table and at the right side of the table, exposure time gotten from DICOM images and calculated cumulative equivalent doses during imaging.*

| **Experiment** | **Dose rate at distance 1.5 m on the end of the patient table** | **Dose rate at distance 0.5 m on the side of the patient table** | **Exposure time** | **Cumulative equivalent dose at distance 1.5 m** | **Cumulative $H_p(10)$ equivalent dose at distance 0.5 m** |
|---|---|---|---|---|---|
| Pelvis AP adult | 1336 µSv/h | 14720 µSv/h | 45 ms | 16.7 nSv | 184.0 nSv |

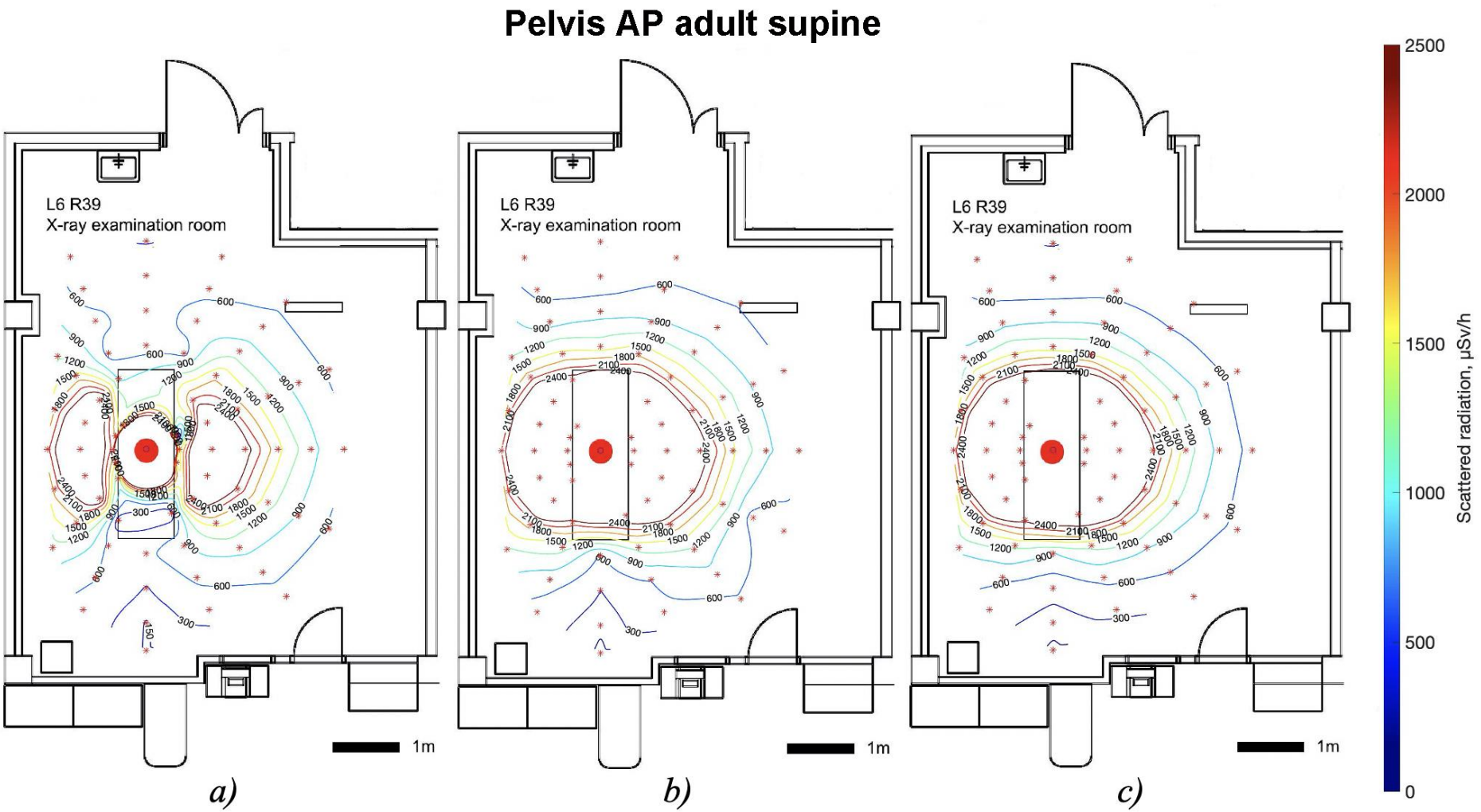


***Figure 24.*** *Scattered radiation maps acquired with a stationary CR by using adult's Pelvis AP imaging program with the phantom placed in supine position. Scattered radiation is presented for heights a) 50 cm, b) 80 cm and 110 cm.*

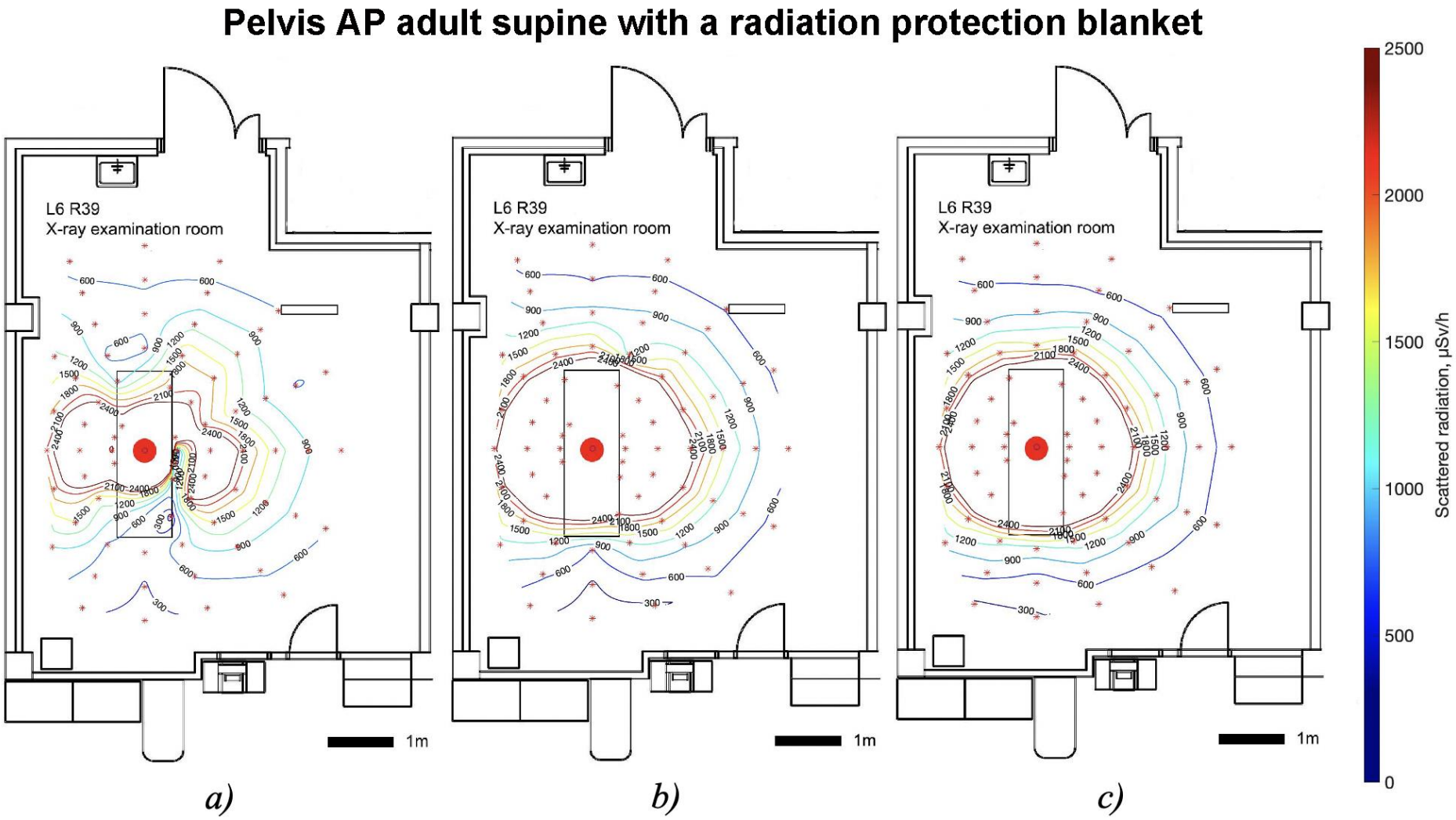


***Figure 25.*** *Scattered radiation maps acquired with stationary CR by using adult's Pelvis AP imaging program with the phantom placed in supine position with a radiation protection blanket placed to cover the chest area. The chest is positioned on the lower part of the patient table in the images. Scattered radiation is presented for heights a) 50 cm, b) 80 cm and 110 cm.*

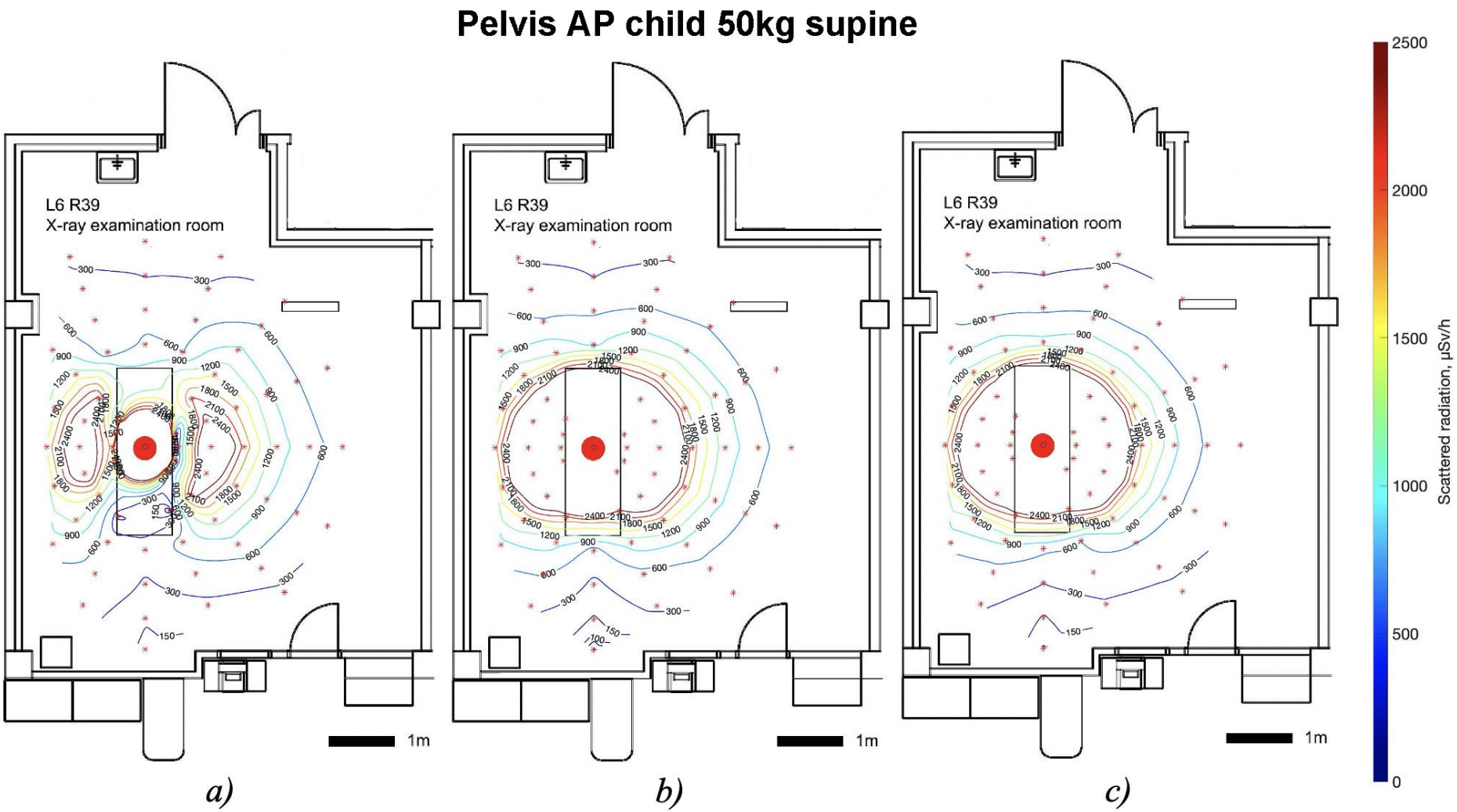


***Figure 26.*** *Scattered radiation maps acquired with stationary CR by using 50kg child's Pelvis AP imaging program with the phantom placed in supine position. Scattered radiation is presented for heights a) 50 cm, b) 80 cm and 110 cm.*

Urological experiment fluoroscopy with mobile fluoroscope

*Figure 27* presents scatter maps acquired with a mobile fluoroscope by using the Ureteral stent insertion -imaging program with the phantom placed in a supine position. In this figure the scattered radiation is presented at the heights of 70 cm, 105 cm and 140 cm, of which the first is lower than the patient table surface. The most prominent feature of these scatter maps is that the scatter is directed to all directions around the phantom, with slight gradual increase in dose rates when comparing values of upper parts of the figures to the lower parts of the figures. The highest dose values were measured on the lower end of the operating table, where the operating physician would be sitting. On the other hand, lowest dose values were measured on the opposite end of the operating table.

*Figure 28* presents scatter maps acquired with a mobile fluoroscope by using the Ureteral stent insertion -imaging program with the phantom placed in a supine position and a lamella radiation protection curtain attached to the end of the operation table. In this figure the scattered radiation is presented at the heights of 70 cm, 105 cm and 140 cm. Features of 105 cm and 140 cm height maps are equivalent to the maps described in previous chapter and presented on the *figure 27.* When the dose rate values of the 70 cm height maps of *figures 27* and *28* are compared, it is evident that the dose values of the end of the operation table, where the lamella radiation protection curtain is positioned, are decreased in *figure 28*.

During urological experiment the operating physician and the anaesthesiologist can be exposed to scattered radiation, when fluoroscopy is used. The operating physician will be positioned most likely on the lower end of the operating table (on the figures) and anaesthesiologist on the place marked on the figures. *Table 9* comprises measured dose rates at these spots and cumulative dose during procedure with the overall fluoroscopy times of 30 seconds and 1 minute.

***Table 9.*** *Estimating the dose of an operating physician and an anaesthesiologist during fluoroscopy guided urological experiment. Table presents measured dose rates at the height of 105 cm at the position of the operating physician and the anaesthesiologist, and the cumulative dose values with overall fluoroscopy times of 30 s and 1 min.*

| | **Physician at distance 0.5 m** | **Anaesthesiologist at distance 1.5 m** |
|---|---|---|
| **Dose rate** | 3634 µSv/h | 70 µSv/h |
| **Cumulative $H_p(10)$ equivalent dose with 30 s fluoroscopy time** | 30.3 µSv | 0.58 µSv |
| **Cumulative $H_p(10)$ equivalent dose with 1 min fluoroscopy time** | 60.6 µSv | 1.17 µSv |

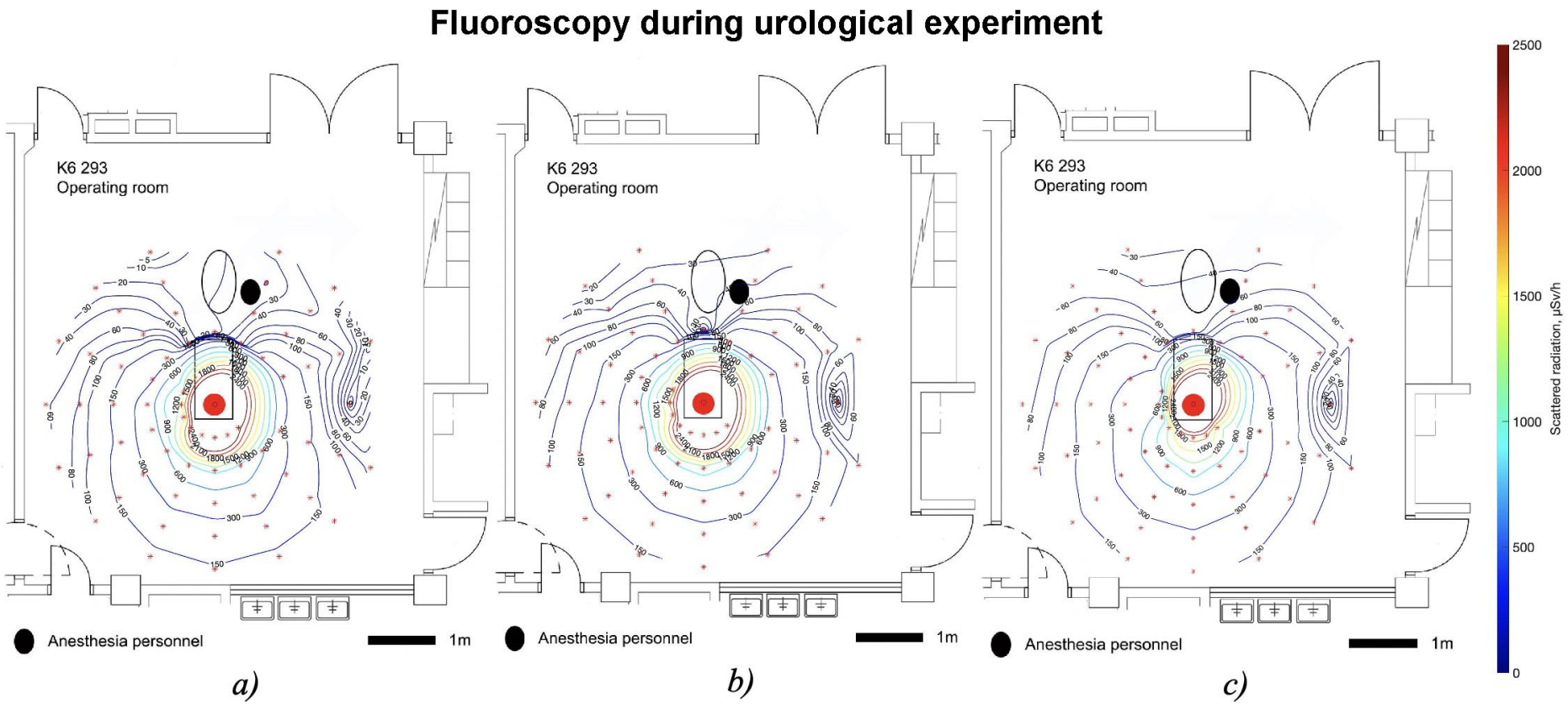


***Figure 27.*** *Scattered radiation maps acquired with mobile fluoroscope by using Ureteral stent insertion -imaging program with the phantom placed in supine position. Scattered radiation is presented for heights a) 70 cm, b) 105 cm and c) 140 cm.*

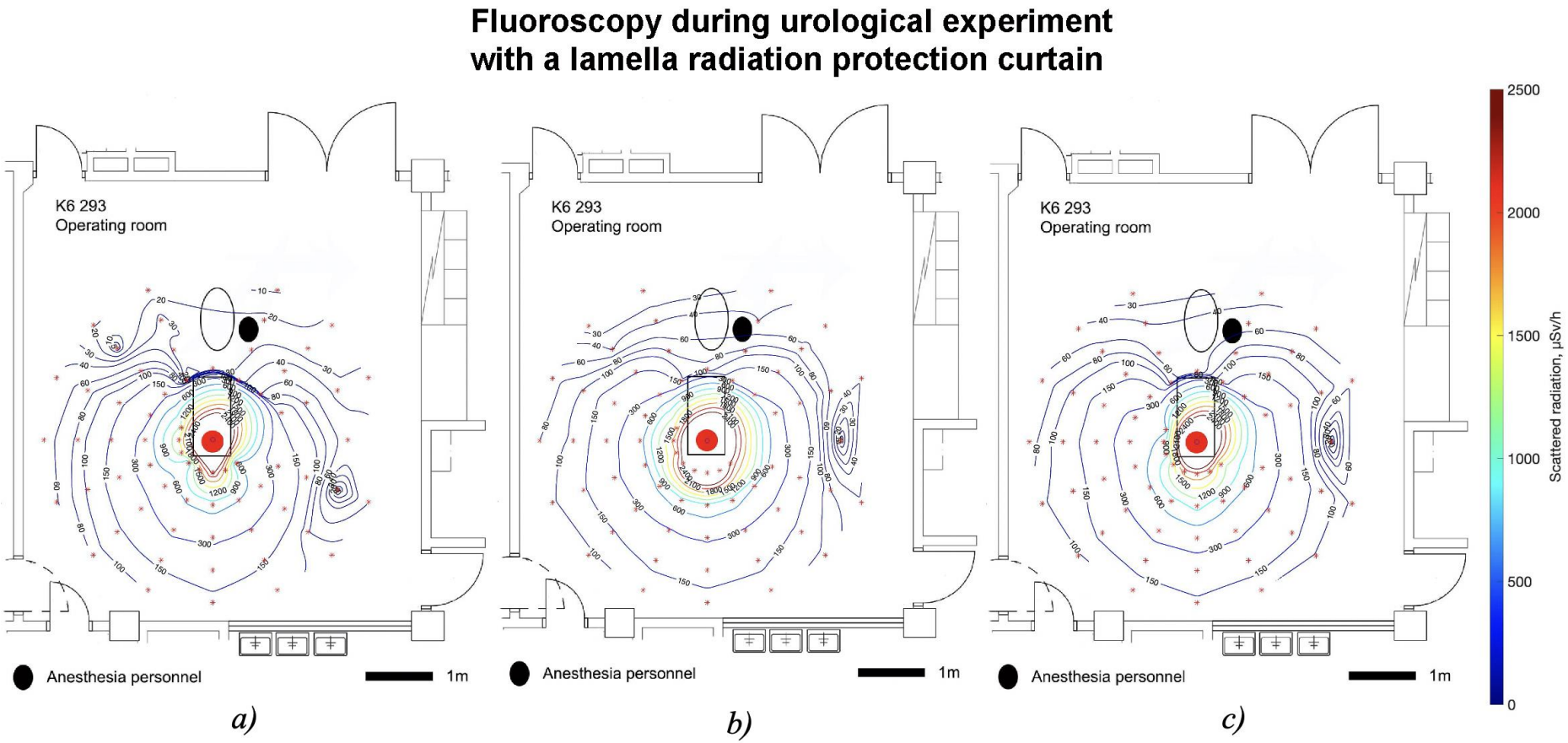


***Figure 28.*** *Scattered radiation maps acquired with mobile fluoroscope by using Ureteral stent insertion -imaging program with the phantom placed in supine position and a lamella radiation protection curtain attached to the lower end of the operation table. Scattered radiation is presented for heights a) 70 cm, b) 105 cm and c) 140 cm.*

Thorax AP with mobile DR

*Figure 29* presents scatter maps acquired with a mobile DR device using the adult's Thorax AP imaging program with the phantom placed in a supine position. In this figure scattered radiation is presented at the heights of 105 cm, 135 cm and 165 cm. The most prominent feature of these maps is that the scattered radiation is directed quite equally to all directions around the phantom, excluding the slight deviations seen on the 105 cm height map. When comparing the dose rate values to supine Pelvis AP scatter maps (*Figure 24*), it is evident that dose rate values of the scattered radiation are distinctly lower in supine Thorax AP images taken with a mobile DR.

In addition to the patient other people may be exposed to scattered radiation during bedside Thorax AP supine imaging with mobile DR. In the general situation the mobile DR device is used in different wards to image patients that can't be moved and therefore other patients are on the same room during imaging. *Table 10* comprises scattered radiation highest values measured on distances 0.5 m and 1 m from the centre of scattering object. Table also includes used exposure time and cumulative doses calculated based on it.

***Table 10.*** *Estimating dose values of other people remaining in imaging room during supine Thorax AP with mobile DR. Table presents highest detected dose rates at the height of 135 cm at distances of 0.5, 1 and 1.6 m, used exposure time and cumulative doses calculated based on the previous two.*

| | **Distance 0.7 m** | **Distance 1 m** | **Distance 1.6 m** |
|---|---|---|---|
| **Experiment** | Thorax AP adult | Thorax AP adult | Thorax AP adult |
| **Exposure time** | 3 ms | 3 ms | 3 ms |
| **Highest detected dose rate** | 579 µSv/h | 353 µSv/h | 193 µSv/h |
| **Cumulative $H_p(10)$ equivalent dose** | 0.483 nSv | 0.294 nSv | 0.161 nSv |

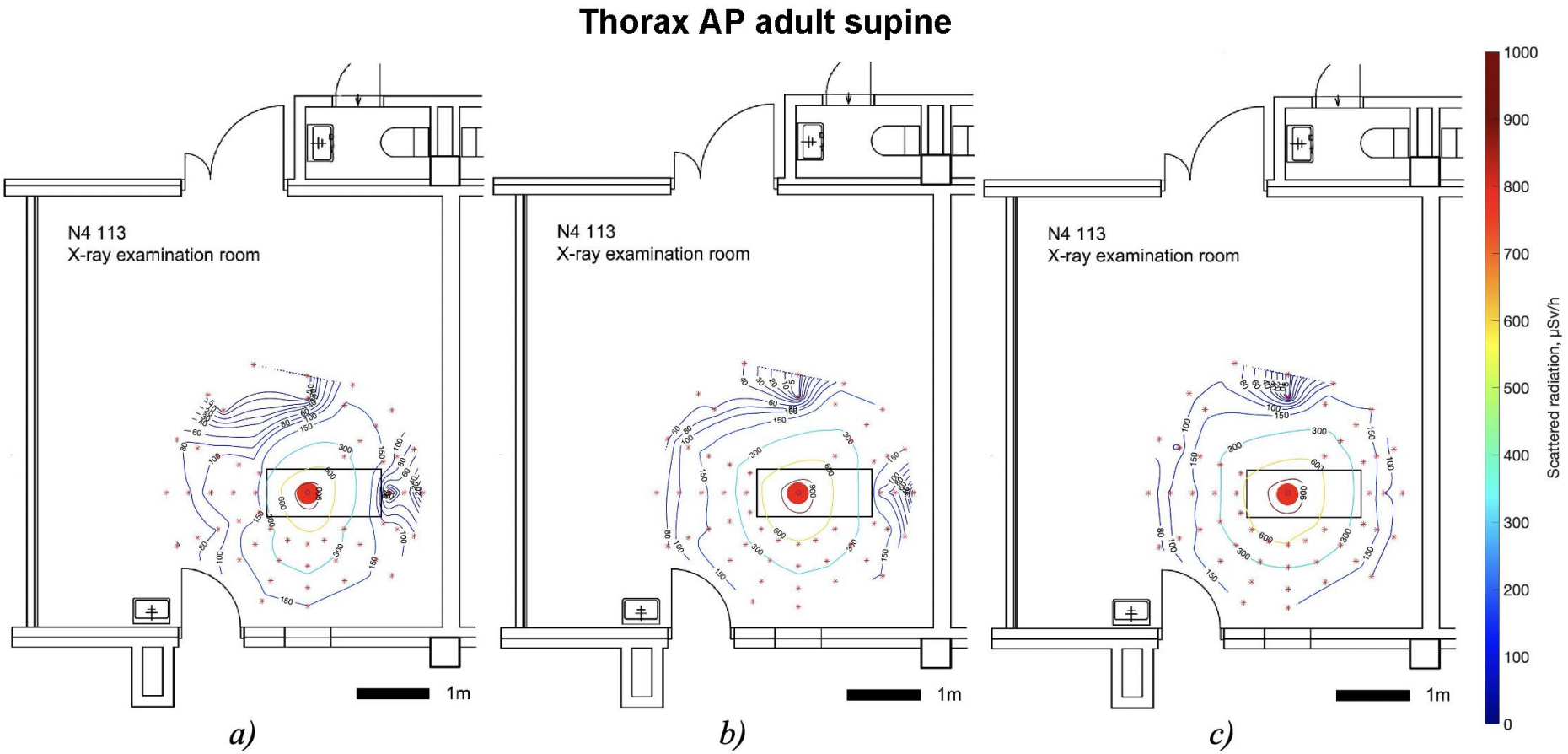


***Figure 29.*** *Scattered radiation maps acquired with a mobile DR device by using adult's Thorax AP imaging program with the phantom placed in supine position. Scattered radiation is presented for heights a) 105cm, b)135cm and 165cm.*

## 2. Reliability of the results

Reliability of the chosen measurement method was evaluated by repeating measurement ten times in three points. Consecutive measurements were done at intervals of 2-5 minutes and the dosimeter holder was repositioned after each measurement. Repeatability measurements were implemented in the children's X-ray experiment room L6 R39 in angular point 45° (*Figures 18 and 19*) and at the distance of 1.0 m from the center of the scattering object using the standing Thorax PA adult imaging program. *Figure 30* illustrates the position of the measurement point in respect to the centre of the scatter origin inside the phantom, i.e. respect to the primary beam field centre point inside phantom.

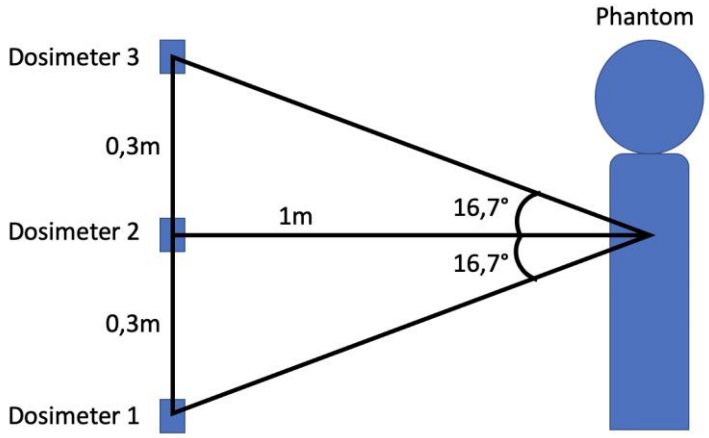


***Figure 30.*** *Illustration of the dosimeter positions in respect to the centre point of the scatter origin inside phantom. Scatter is generated mostly in the parts of phantom that is on the field of the x-ray primary beam.*

Results of the repeatability measurements are presented in the *table 11.* Mean dose rate values of dosimeters at the heights 105, 135 and 165 cm were 1104.3, 1017.4 and 945.2 µSv/h, respectively. In the same order standard deviations of dosimeter values were 178.8, 49.0 and 188.9 µSv/h. These values imply that the dispersion of measured values is greater on the dosimeters 1 and 3 with respect to dosimeter 2 that is aligned at the same height as the x-ray primary beam centre axes.

To better evaluate the relative dispersion of each dosimeter a coefficient of variation (*CV*) was determined by using formula:

$$CV = \frac{S}{\bar{x}} \times 100\% \qquad [7]$$

where $S$ is the standard deviation and $\bar{x}$ is the mean. Obtained CV values are presented on the *table 12.* (Sokal R.R. & Rohlf F.J. 1987, Suchmacher M. & Geller M. 2012)

In general CV values of < 15 % are considered to represent low dispersal, values of 15 % to 30 % average dispersal and values > 30 % high dispersal (Suchmacher M. & Geller M. 2012). Obtained CV values for dosimeters 1, 2 and 3 were 16 %, 5 % and 20 %, respectively. Consequently dosimeter 2 values can be considered to have a low dispersal, and dosimeters 1 and 3 values an average dispersal.

Manufacturer has specified the angular dependence of the dosimeter. The angular dose rate accuracies are +/- 5 % and +/- 30% for angles of +/- 5° and +/- 50°, respectively (*Table 13*). In the repeatability measurements middle one of the dosimeters (dosimeter 2) was positioned close to 0° and two other dosimeters (dosimeter 1 and 3) were positioned in +/- 16.7° angles with respect to the horizontal plane on the level of the primary beam central axes. Therefore, the middle one of the dosimeters should have lowest dispersion. Obtained CV values are convergent with this presumption.

The measured maximum and minimum values with respect to the mean value for dosimeters 1, 2 and 3 were 127.0 %/79.6 %, 109.9 %/94.6 % and 125.2 %/74.7 %, respectively (*Table 11*). Measured maximum and minimum values of dosimeters 1 and 3 comply with the manufacturer angular dependence specifications (*Table 13*), but dosimeter 2 doesn't.

It can be concluded that the best measurement accuracy is achieved with the dosimeter that is positioned on the same horizontal plane with the primary beam central axes, as this dosimeter has the lowest CV value. However, the dispersion of this dosimeter is higher than manufacturer has specified, when measured maximum and minimum values respect to the mean value are considered. Reason for this could be that the used dosimeter system is close to its lifetime limit, which is according to manufacturer 3-5 years. (Unfors Raysafe AB 2020)

***Table 11.*** *Results of the repeatability measurements.*

| | **Dosimeter 1, 105cm [µSv/h]** | **Dosimeter 2, 135cm [µSv/h]:** | **Dosimeter 3, 165cm [µSv/h]** |
|---|---|---|---|
| **1. measurement** | 1402 | 968 | 1077 |
| **2. measurement** | 1355 | 966 | 1183 |
| **3. measurement** | 1267 | 962 | 1139 |
| **4. measurement** | 1155 | 991 | 1180 |
| **5. measurement** | 992 | 1021 | 987 |
| **6. measurement** | 1019 | 1023 | 855 |
| **7. measurement** | 952 | 1035 | 788 |
| **8. measurement** | 992 | 1026 | 706 |
| **9. measurement** | 1012 | 1118 | 781 |
| **10. measurement** | 897 | 1064 | 756 |

| | | | |
|---|---|---|---|
| **Mean** | 1104.3 | 1017.4 | 945.2 |
| **Standard deviation** | 178.8 | 49.0 | 188.9 |
| **Minimum (in percents with respect to mean)** | 879 (79.6 %) | 962 (94.6 %) | 706 (74.7 %) |
| **Maximum (in percents with respect to mean)** | 1402 (127.0 %) | 1118 (109.9 %) | 1183 (125.2 %) |

***Table 12.*** *Coefficient of variation of each dosimeter.*

| | **Dosimeter 1, 105cm** | **Dosimeter 2, 135cm** | **Dosimeter 3, 165cm** |
|---|---|---|---|
| **Coefficient of variation** | 16% | 5% | 20% |

***Table 13.*** *Calibration values of the RaySafe i2 dosimeter stated by the manufacturer. These values limit the measurement accuracy of the dosimeter.*

| **Operational Quantity** | **$H_p(10)$** |
|---|---|
| **Dose rate range and linearity** | +/- 10 % 40 μSv/h – 150 mSv/h<br>+/- 20 % 150 mSv/h – 300 mSv/h |
| **Energy dependence x-, γ-rays** | +/- 20 % within N40 – N100<br>+/- 30 % within N100 – N120 |
| **Angular dependence** | +/- 5 % within +/- 5 °<br>+/- 30 % within +/- 50 °<br>+ 200 % / -100 % within +/- 90 ° |
| **Temperature dependence** | +/- 5 % within 20 – 26 °C<br>+/- 25 % within 15 – 35 °C |

# Discussion

The purpose of this research was to find out spatial distribution of the scattered radiation in the experiment or the operation room during Thorax PA and LAT radiography, Pelvis AP radiography, fluoroscopy guided urological experiment and bedside Thorax AP radiography using stationary DR, stationary CR, mobile fluoroscope and mobile DR, respectively. Additionally, the aim was to estimate effective doses of the staff, that remain on the room during imaging and are therefore exposed to ionizing radiation.

Literature review reveals that there are very few wide direct dose rate measurements published previously during the last decade, which limits the analysis of the results. Literature published before 2010 is not comparable because of the fast development of the X-ray imaging in the 20th century. Publications found from the recent years are either simulated (Rodas N.L. & Padoy N. 2015, Süncksen M. et al. 2020), were done using different measurement technique, less measurement points or using different imaging program (Abrantes A. et al. 2015, Ardiatna W. et al. 2020, Chiang H-W et al. 2020, Chida K. 2011, Nakamura T. et al. 2019, Nowak M. et al. 2020, Santos J. S. et al. 2020, Struelens L. et al. 2011), and therefore they are also not fully comparable. Many publications regarding healthcare staff dose values have been implemented also by measuring doses during real interventional operations and so they provide cumulative point like information of the scattered radiation doses of the staff (Apelmann C. et al. 2019, Kwang P.K. et al. 2012, Miraglia R. et al. 2017, Rivera-Montalvo T. & Uruchurtu-Chavarin E.S. 2020, Sciahbasi A. et al. 2018).

Other limitation of the research is due to the chosen measurement method. As dosimeters were attached on the infusion stand during measurements, the highest and lowest dosimeter were not perpendicular to the coming scattered radiation. This limits the reliability of the results gotten with these dosimeters, as the manufacturer of dosimeters have stated, that the dosimeters are angularly dependent. Therefore, the results gotten with the centremost dosimeter can be considered the most reliable, as it was positioned in all measurements on the same horizontal level with the scatter origin. This is also supported by the lowest standard deviation and the lowest coefficient of variation results gotten for the centremost dosimeter on the reliability tests.

In this research, the main goal was to implement wider scattered radiation maps that could be used in training of radiation workers. Maps concretize the inverse square law to radiation workers, as they are actually able to see how significantly the intensity of the scattered radiation decreases with the

increasing distance to the scattered radiation source (i.e. patient). Maps also reveal possible low scatter areas in situations where the distribution of scattered radiation is unequal in all directions.

The first series of maps were measured using standing Thorax PA and LAT imaging programs. It is evident that in all of these maps, the scattered radiation field is strongly emphasized from the phantom towards the X-ray tube and highest dose values are achieved with the centre most dosimeter that is positioned on the same horizontal plane with the primary beam centre axes. This is convergent with the publication of Jentzsch et al. (2015), where they stated that "highest scattered radiation is located on the side where the X-ray beam enters the patient". These maps also reveal that the scattered radiation intensity in Thorax LAT projection is higher in comparison to Thorax PA. This is also in accordance with the publication of Jentzsch et al. (2015), where they stated regarding staff exposure that "second way to decrease radiation exposure is to position C-arm antero-posteriorly because this is associated with much less radiation exposure than lateral X-rays".

The second series of maps were measured using supine Pelvis AP imaging program. It is evident that in all of these maps at hights of 80 cm and 110 cm the scattered radiation is quite equally distributed in all directions. These are convergent with the publication of Rodas N.L. & Padoy N. (2015), where they visualized propagation of intraoperative scattered radiation by using simulation and wireless dosimeters. On the other hand, maps that were measured at the hight of 50 cm differ from others and are quite complex in nature. Reason for this is probably the metallic structures of the patient table that attenuate the scattered radiation unevenly.

On one of the Thorax series measurements a pelvic shield was dressed on the phantom and on one of the Pelvis series measurements a radiation protective blanket was used to cover chest area of the phantom. The use of the shield did not affect the scattered radiation at either of the cases at the heights measured. This is expected, as the shield was positioned on the surface of the phantom outside of the primary beam and so the scattered radiation is directed parallel to the shield surface past it.

One of the Thorax measurements and one of the Pelvis measurements were done using 50 kg child's imaging program and setup parameters. Contrary to what was expected, the maps implemented using this program did not differ from the ones gotten with the adult's program. Reasons for this might be that the same phantom was used in all measurements and that manual control was used in child's measurements whereas automatic control was used in adults. More reliable comparison could be done, if measurements were redone using a phantom corresponding better to the child's body.

The third series of maps were measured using fluoroscopy with the Ureteral stent insertion -imaging program. It is evident that the scattered radiation is directed to all directions with emphasis towards the end of the patient table where the physician would be sitting during the operation. On the other hand, the scattered radiation values of the opposite end of the table appear to be smaller. Reason for this might be that most of the patient's body is on this side of the scatter origin and so the scattered radiation is partly attenuated by the patient's body.

In second fluoroscopy measurement series a radiation protective lamella curtain was used at the end of the operation table, where the operating physician is positioned during procedure. It is evident that this curtain decreases the scattered radiation doses measured with the lowest dosimeter at the height of 70 cm at the end of the table. But as the curtain did not fit perfectly on the table and the lamellas did not go perfectly between each other, there is a peak on the dose values on the centre of table end. This corresponds to the point where there was an opening between the lamellas. This shows that correct positioning of the radiation protective gear is essential.

The fourth series of maps were measured using the supine Thorax AP imaging program and mobile digital radiography. It is evident that the scattered radiation is directed quite equally to all directions, as in the supine Pelvis AP measurements, and that the measured dose values are the lowest of all measurements. The low dose values are both expected and desirable, as the mobile DR system is used for the bedside radiology in different hospital wards where several people can be present on the room during imaging, including other patients. The measured values at height 135 cm and at distances 0.7 and 1 m are convergent with the values gotten by Abrantes A. et al. (2017) in their research, where they measured scatter radiation exposure during mobile bedside X-ray examinations. It should be noted that the imaging system and parameters they used were different and so the results are not fully comparable.

As it was explained on the theory chapter (chapter 3.1.1), the cumulative dose value of the $H_p(10)$ dosimeter, can be used as an estimate of the effective dose. Measured cumulative dose values of the assisting person were 5.17 nSv and 47.5 nSv at the height of 135 cm at 0.5 m distance in Thorax AP and Thorax LAT projections, respectively. These values represent 0.000026 % and 0.00024 % of the annual effective dose limit of the radiation workers, that is 20 mSv, respectively. Additionally, values are equal to 133 and 1221 seconds of background radiation, respectively, as during measurements on spring 2020 the background radiation was ~0.140 μSv/h on the closest measurement point at Raksila

(STUK 2020a). Corresponding cumulative values for Pelvis AP were 184.0 nSv at the height of 80 cm at distance 0.5 m at the side of the patient table and 16.7 nSv at distance 1.5 m at the end of the patient table. These values represent 0.00092 % and 0.000084 % of the annual dose limit of the radiation workers and are equal to 4731 and 429 seconds of background radiation, respectively. Therefore, the dose received by the assisting person during these experiments is small when compared to the yearly dose limit of radiation workers. However, to decrease exposure it is advisable for assisting person to keep bigger distance than 0.5 m to the patient especially on standing Thorax LAT projection, and to position oneself on the end of the patient table on supine Pelvis AP projection.

Measured cumulative effective dose values of the operating physician at the height of 105 cm and at the distance of 0.5 m during urological experiment with total fluoroscopy times of 30 seconds and 1 minute were 30.3 µSv and 60.6 µSv, respectively. When comparing to the annual effective dose limit, these values represent 0.151 % and 0.303 % of it, respectively, and so the annual dose limit would be exceeded if the physician would perform 660 and 330 analogous operations in a year, respectively. On the other hand, when compared to the background radiation, these values are equal to 9 and 18 days of background radiation. Corresponding dose values for anaesthesiologist standing at the distance 1.5 m from the scatter origin were 0.58 µSv and 1.17 µSv, which represent 0.003 % and 0.006 % of the annual dose limit and are equal to 4 and 8 hours of background radiation, respectively. Therefore, doses received by the anaesthesiologist are quite small when compared to the operating physician. Estimated physician's effective doses are high, as the value represents situation where the physician is positioned 0.5-meter distance from the primary beam central axes. In practice, it is likely that the distance to the scattered radiation origin is increased and radiation protection equipment is exploit.

According to Medical Physicist Tuija Keinänen (personal communication, January 25th, 2021) the number of Ureteral stent insertion -operations were 44 and 55 during years 2018 and 2019, respectively. In these operations the same imaging program was used as in the implemented scatter radiation measurements. Additionally, during same years the number of other ureteral stent related operations, including stent removals and replacements, were 62 and 70, respectively. The fluoroscopy time being in all ureteral stent operations mainly under 1 minute. If on year 2019 same physician would have performed all 125 ureteral stent related operations, the estimate of cumulative effective dose would have been 3.8 and 7.6 mSv with average fluoroscopy times of 30 s and 1 min per operation, respectively. Therefore, yearly effective dose limit of 20 mSv would not have been exceeded.

Measured cumulative dose values at the height of 135 cm and at distances of 0.7 m and 1 m during supine bedside Thorax AP projections were 0.483 nSv and 0.294 nSv, respectively. These values represent 0.0000024 % and 0.0000015 % of the annual effective dose limit of the radiation workers, respectively. Additionally, values are equal to 12.4 and 7.6 seconds of background radiation, respectively. Therefore, it is evident, that the dose received by the healthcare personnel staying in the room during imaging is small. As there might also be other patients in the room during imaging, it is essential to estimate their exposure during imaging. The position of other patients with respect to the X-ray examined patient can vary, but for estimation purposes assumption is taken that the distance between patients is 1.6 meters. The maximum measured dose rate value during bedside Thorax imaging at the distance of 1.6 m was 193 µSv/h. As the used exposure time was 3 ms the cumulative dose during imaging at distance of 1.6 m would be 0.161 nSv, which is equal to 4.2 seconds of background radiation. Consequently, the effective dose received by other patients is small and they can safely stay on the room during imaging.

# Conclusions

The purpose of this research was to implement scattered radiation maps for educational purposes for the radiation protection training, and to estimate radiation exposure of the staff and other patients staying on the imaging room. Literature review revealed that the number of similar wide direct measurements of the scattered radiation is low during the last decade. Completed maps comply with the previous research, however the comparison is limited as in all found scientific articles the used measurement method differs to varying extent from the implemented study.

Maps gotten using lateral X-ray tube demonstrate that the scattered radiation is strongly directed back from the patient towards the X-ray tube. Scatter intensity being stronger in LAT projection compared to PA projection. On the other hand, maps gotten using vertical X-ray tube demonstrate that the scattered radiation is directed quite equally to all directions, when the plane perpendicular to the primary beam central axis is considered. Use of the pelvic shield in standing position and the radiation protection blanket in supine position did not have effect on the maps, and neither did using 50kg child's imaging parameters.

Effective dose estimates of health care personnel are small in all addressed situations in comparison to yearly dose limits set to the radiation workers. Highest doses were gotten for the operating physicians in urological experiment measurements and lowest for personnel conducting bedside Thorax examinations. There is also great difference on the assisting person's dose estimates between standing Thorax PA, standing Thorax LAT and supine Pelvis AP projections. Based on the results, it is recommendable for assisting person to keep higher than 0.5 m distance to the patient on standing Thorax LAT examination and to position oneself on the end of patient table on the supine Pelvis AP projection.

Results demonstrate that the operating physicians are in greatest risk of exceeding the yearly dose limit set by law to the radiation workers. Hence, it would be beneficial to further investigate their effective dose in various situations to uncover possible differences on the dose in different types of operations. Additionally, if in future a child corresponding dosimetry verification phantom would come available to use, it would be beneficial to redo the measurements which were done using child's imaging program. Implemented study did not find major differences on the scattered radiation between child's and adult's examination, as the same phantom was used in both. More reliable results could be achieved if a phantom better equal to child's body would be used.

# References


Abrantes A., Rebelo C., Sousa C. & Rodrigues S. (2017). Scatter Radiation Exposure During Mobile X-Ray Examinations. HealthManagement, 17 (1), 68-72.

Alpen E.L. (1998). Radiation Biophysics, 2nd edition. California, San Diego: Academic Press.

Als-Nielsen J. & McMorrow D. (2011). Elements of Modern X-Ray Physics, 2nd edition. Singapore: Markono Print Media Pte Ltd.

Alzen G. & Benz-Bohm G. (2011). Radiation protection in Pediatric Radiology. Deutsches Ärzteblatt International, 108(24), 407-414.

Anonymous (1896). Professor Routgen's wonderful discovery. New York, Scientific American, 25.1.1896.

Apelmann C., Kowald B., Weinrich N., Dischinger J., Nienhaus A., Seide K., Martens H. & Jurgens C. (2019) Radiation dose to the eye lens through radiological imaging procedures at the surgical workplace during trauma surgery. International journal of environmental research and public health, 16, 3850.

Ardiatna W., Pratiwi N.G., Pawiro S.A., Wigati K.T. and Soejoko D.S. (2020). Influence of Various Setup Parameters on Scattered Fraction in Interventional Cardiology. Journal of Physics: Conference series, 1505, 012042.

Arshak K. & Korostynska O. (2006) Advanced Materials and Techniques for Radiation Dosimetry. Norwood, MA: Artech House.

Bartal G., Vano E., Paulo G. & Miller D.L. (2014) Management of patient and staff radiation dose in interventional radiology: Current concepts. Cardiovasc Intervent Radiol, 37, 289-298.

Carroll Q.B. (2018). Radiography in the Digital Age. Springfield, Illinois: Charles C Thomas Publisher LTD.

Cherry S. R., Sorenson J.A. & Phelps M.E. (2012). Physics in Nuclear Medicine, 4th edition. W B Saunders Co Ltd.

Chiang H-W., Chiang H-J., Li J-H. & Tsang L.L-C. (2020) Evaluation of scattered radiation dose received by medical staff during uterine artery embolization in the operating room. Technology and health care, 28, 3-11.

Chida K., Kaga Y., Haga Y., Kataoka N., Kumasaki E., Meguro T. and Zuguchi M. (2012). Occupational dose in interventional radiology procedures. American journal of roentgenology, 200 (1), 138-141.

Chida K., Takahashi T., Ito D., Shimura H., Takeda K. & Zuguchi M. (2011) Clarifying and visualizing sources of staff-received scattered radiation in interventional procedures. American journal of roentgenology, 197, W900-W903.

Dance D.R., Christofides S., Maidment A.D.A., McLean I.D. and NG K.H. (2014). Diagnostic radiology physics. A handbook for teachers and students. Vienna, Austria: International atomic energy agency.

Ehrlich R.A. & Coakes D.M. (2017). Patient care in radiography. With introduction to medical imaging. St. Louis, Missouri: Elsevier.

Eur-lex (2020, November 23rd) Council directive 2013/59/EURATOM. Retrieved from https://eur-lex.europa.eu/eli/dir/2013/59/oj

Finlex (2020a, October 13th). Finnish government regulation 1034/2018. Retrieved from https://www.finlex.fi/fi/laki/alkup/2018/20181034#Pidp446486576

Finlex (2020b, October 29th). Radiation law 859/2018. Retrieved from https://finlex.fi/fi/laki/alkup/2018/20180859#Pidp445992960

Franklin K., Muir P., Scott T., Wilcocks L. & Yates P. (2010). Introduction to Biological Physics for the Health and Life Sciences. United Kingdom: Wiley.

IAEA (2012). Radiation protection in paediatric radiology. Vienna.

IAEA (2020a, October 15th) Good practices in interventional fluoroscopy. Retrieved from https://www.iaea.org/resources/rpop/health-professionals/interventional-procedures/good-practices-in-interventional-fluoroscopy

IAEA (2020b, October 26th) 10 Pearls: Radiation protection of patients in fluoroscopy. Retrieved from https://www.iaea.org/sites/default/files/documents/rpop/poster-patient-radiation-protection.pdf

IAEA (2020c, October 26th) 10 Pearl: Radiation protection of staff in fluoroscopy. Retrieved from https://www.iaea.org/sites/default/files/documents/rpop/poster-staff-radiation-protection.pdf

Jantunen H., Kortelainen K., Lehkonen M. & Wood P. (2006). Henkilökunnan ja potilaan säteilysuojelu lääketieteellisessä säteilyn käytössä. Suomen Röntgenhoitajaliitto ry. Tampere, Finland: Hämeen Offset-tiimi Oy.

Jentzsch T., Pietsch C.M., Stigler B., Ramseler L.E., Seifert B. & Werner C.M.L. (2015) The compliance with and knowledge about radiation protection in operating room personnel: a cross-sectional study with a questionnaire. Arch Orthop Trauma Surg., 135 (9), 1233-1240.

Järvinen H., Eskola M., Hallinen E., Järvinen J., Kivelä A. et al. (2018). Säteilyn käytön turvallisuus kardiologiassa. Säteilyturvakeskus.

Kabir M.Z. & Kasap S. (2017) Photoconductors for X-ray Image Detectors. In: Kasap S. & Capper P. (eds) Springer Handbook of Electronic and Photonic Materials. Springer International Publishing AG.

Kwang P.K., Miller D.L., Berrington de Gonzalez A., Balter S., Kleinerman R.A., Ostroumova E., Simon S.L. and Linet M.S. (2012). Occupational radiation doses to operators performing fluoroscopically-guided procedures. Health Phys., 103 (1), 80-99.

Martz H.E. Jr., Logan C.M., Schneberk D.J. & Shull P.J. (2017). X-ray imaging. Fundamentals, industrial techniques and applications. DRD Press.

Mettler F.A. Jr. (2018). Medical radiation exposure in the United States: 2006-2016 trends. Health Phys., 116 (2), 126-128.

Mikla V. & Mikla V. (2014). Medical imaging technology. Elsevier.

Miller D.L., Vano E., Bartal G., Balter S., Dixon R., Padovani R., Schueler B. & Cardella J.F. (2010) Occupational radiation protection in interventional radiology: A joint guideline of the cardiovascular and Interventional Radiology Society of Europe and the Society of Interventional Radiology. Cardiovasc Intervent Radiol, 33, 230-239.

Miraglia R., Gerasia R., Maruzzelli L., D'Amico M. & Luca A. (2017) Radiation doses to operators performing transjugular intrahepatic portosystemic shunt using a flat-panel detector-based system and ultrasound guidance for portal vein targeting. European Society of radiology, 27, 1783-1786.

Nakamura T., Scoichi S., Takei Y., Cruz V., Kobayashi I., Asegawa S. and Kato K. (2020) A more accurate and safer method for the measurement of scattered radiation in x-ray examination rooms. Radiological physics and technology, 13, 69-75

Nicholls M. (2019). Wilhelm C. Röntgen discoverer of X-rays. European Heart Journal, 40 (20), 1584-1586.

Nowak M., Carbonez P., Krauss M., Verdun F.R. and Damet J. (2020) Characterisation and mapping of scattered radiation fields in interventional radiology theatres. Scientific reports, 10:18754.

Radon J. (1986). On the determination of function from their integral values along certain manifolds. Translated by P.C. Parks from the original German text. IEEE Transactions on Medical Imaging, 5 (4), 170-176.

Rivera-Montalvo T. & Uruchurtu-Chavarin E.S. (2020) Scattered radiation on cardiologists during interventional cardiac procedures. Radiation physics and chemistry, 167, 108274.

Rodas N.L. & Padoy N. (2015) Seeing is believing: increasing intraoperative awareness to scattered radiotion in interventional procedures by combining augmented reality, Monte Carlo simulations and wireless dosimeters. Int J CARS, 10, 1181-1191.

Roguin A., Goldstein J., Bar O., & Goldstein J.A. (2013) Brain and neck tumors among physicians performing interventional procedures. Am J Cardiol., 111, 1368-1372.

Ruonala V. (2019) Radiologisten tutkimusten ja toimenpiteiden määrät vuonna 2018. STUK-B 242. Helsinki.

Röntgen W.C. (1896). On a new kind of rays. Nature, 53, 274-276.

Saarakkala S., Kaleva E., Kauppinen E. & Töyräs J. (2007) Evaluation of X-ray Scattering in Examination Room During Routine Radiography. Radiological Society of North America 2007 Scientific Assembly and Annual Meeting. Chicago, Illinois.

Santos J.S., Uusi-Simola J., Kaasalainen T., Aho P. & Venermo M. (2020) Radiation doses to staff in a hybrid operating room: An anthropomorphic phantom study with active electronic dosimeters. Eur J Vac Endovasc surg, 59, 654-660.

Sciahbasi A., Sarandrea A., Rigattieri A., Patrizi R., Cera M., Di Russo C., Perone F., Porretta V., Fedele S., Romano S., Penco M. & Ferraiuolo G. (2018) Staff radiation dose during percutaneous coronary procedures: Role of adjunctive protective drapes. Cardiovascular revescularizatino medicine, 19, 755-758.

Sequeiros R.B., Koskinen S., Aronen H., Lundbom N., Vanninen R. & Tervonen O. (2017). Kliininen radiologia. Helsinki, Finland: Kustannus Oy Duodecim.

Siiskonen T. (2020). Suomalaisten keskimääräinen efektiivinen annos vuonna 2018. Säteilyturvakeskus-A263. Helsinki, Finland.

Smith W.L. & Farrell T.A. (2014) Radiology 101. The basics and fundamentals of imaging. 4th edition. USA, Philadelphia: Wolters Kluwer / Lippincott Williams & Wilkins Health.

Sokal R.R. & Rohlf F.J. (1987) Introduction to biostatistics, 2nd edition. New York: W.H. Freeman and Company.

Spahn M. (2013). X-ray detectors in medical imaging. Nuclear instruments and methods in physics research A, 731, 57-63.

Statkiewicz Sherer M.A., Visconti P.J., Russell Ritenour E. & Welch Haynes K. (2018). Radiation protection in medical radiography, 8th edition. St. Louis, Missouri: Elsevier.

Struelens L., Kauwenberghs K. & Vanhavere F. (2011) Characterization of the scattered radiation field around an x-ray tube. Phys. med. biol., 56, 2731-2741.

STUK (2018). Säteilyn käytön turvallisuus kardiologiassa. Helsinki.

STUK (2011). Säteilynlähteiden käyttötilojen suunnittelu. ST 1.10. Helsinki.

STUK (2009). Säteilyn terveysvaikutukset. Helsinki, Finland: Vammalan kirjapaino.

STUK (2004). Säteily- ja ydinturvallisuus -kirjasarja: Säteilyn käyttö. Hämeenlinna, Suomi: Karisto Oy:n kirjapaino.

STUK (2020a, November 30th) Radiation situation today. Retrieved from https://www.stuk.fi/aiheet/sateily-ymparistossa/sateilytilanne-tanaan

STUK (2020b, October 10th) Työntekijöiden säteilyaltistus. Retrieved from https://www.stuk.fi/stuk-valvoo/sateilyn-kayttajalle/tyontekijoiden-suojelu-ja-sateilymittaukset/tyontekijoiden-sateilyaltistus

Suchmacher M. & Geller M. (2012) Practical Biostatistics: A User-Friendly Approach For Evidence-Based Medicine. USA: Elsevier.

Süncksen M., Bott O.J., Dresing K. and Teistler M. (2020) Simulation of scattered radiation during intraoperative imaging in a virtual learning environment. International Journal of Computer Assisted Radiology and Surgery, 15, 691-702.

Unfors Raysafe AB (2020, October 11th). RaySafe i2 real-time radiation dosimeter. Retrieved from https://www.raysafe.com/products/real-time-dosimetry-systems/raysafe-i2-real-time-radiation-dosimeter.

Wagner M., Dresing K., Ludwig W., Ahrens C.A. and Bott O.J. (2012) SIScaR-GPU:fast simulation and visualization of intraoperative scattered radiation to support radiation protection training. Stud Health Technol Inform., 180, 968-72.

Wolbarst A.B. (1999). Looking Within: How They Help Physicians Save Lives. California: University of California Press.

Zanzonico P., Dauer L. and Strauss W. (2016). Radiobiology in cardiovascular imaging. JACC: Cardiovascular imaging, 9 (12), 1446-61.